RESEARCH ARTICLE

Correspondence to:
Y. P. Wang,
ypwang@nju.edu.cn

Erosion and Accretion on a Mudflat: The Importance of Very Shallow-Water Effects

Benwei Shi[1,2] iD, **James R. Cooper[3]** iD, **Paula D. Pratolongo[4]** iD, **Shu Gao[5]** iD, **T. J. Bouma[6]** iD, **Gaocong Li[1]** iD, **Chunyan Li[2]** iD, **S.L. Yang[5]** iD, and **Ya Ping Wang[1,5]** iD

[1]Ministry of Education Key Laboratory for Coast and Island Development, Nanjing University, Nanjing, China, [2]Department of Oceanography and Coastal Sciences, Louisiana State University, Baton Rouge, LA, USA, [3]Department of Geography and Planning, School of Environmental Sciences, University of Liverpool, Liverpool, UK, [4]CONICET – Instituto Argentino de Oceanografía, CC 804, Bahía Blanca, Argentina, [5]State Key Laboratory of Estuarine and Coastal Research, East China Normal University, Shanghai, China, [6]NIOZ Royal Netherlands Institute for Sea Research, Department of Estuarine and Delta Systems, and Utrecht University, Yerseke, The Netherlands

Abstract Understanding erosion and accretion dynamics during an entire tidal cycle is important for assessing their impacts on the habitats of biological communities and the long-term morphological evolution of intertidal mudflats. However, previous studies often omitted erosion and accretion during very shallow-water stages (VSWS, water depths < 0.20 m). It is during these VSWS that bottom friction becomes relatively strong and thus erosion and accretion dynamics are likely to differ from those during deeper flows. In this study, we examine the contribution of very shallow-water effects to erosion and accretion of the entire tidal cycle, based on measured and modeled time-series of bed-level changes. Our field experiments revealed that the VSWS accounted for only 11% of the duration of the entire tidal cycle, but erosion and accretion during these stages accounted for 35% of the bed-level changes of the entire tidal cycle. Predicted cumulative bed-level changes agree much better with measured results when the entire tidal cycle is modeled than when only the conditions at water depths of >0.2 m (i.e., probe submerged) are considered. These findings suggest that the magnitude of bed-level changes during VSWS should not be neglected when modeling morphodynamic processes. Our results are useful in understanding the mechanisms of micro-topography formation and destruction that often occur at VSWS, and also improve our understanding and modeling ability of coastal morphological changes.

1. Introduction

Tidal mudflats are intertidal, non-vegetated, soft sediment beds, generally forming a large part of the intertidal zone of estuaries and/or coastal areas (Dyer, 2000; Liu et al., 2013a). They support highly productive ecosystems, providing a habitat for a wide variety of benthic fauna and fish species (Barbier, 2013; Dyer et al., 2000; Ribas et al., 2015), as well as feeding grounds for migrant and wintering birds (Andersen et al., 2006; Eisma, 1998; Le Hir et al., 2000; Ysebaert et al., 2003). In addition to their significant ecological functions (Balke et al., 2014; Bouma et al., 2016; Liu et al., 2013b), the unconsolidated mud on tidal mudflats is known to provide physical shoreline protection by attenuating wave energy in the near-shore region (Bale et al., 2006; Costanza et al., 2008; Gedan et al., 2010; Möller et al., 2001; Temmerman et al., 2012). However, tidal mudflats are currently under threat from human activities and natural stress (Wang et al., 2017), such as large-scale reclamation projects and river damming (e.g., Chung et al., 2004; Dai et al., 2013; French et al., 2000; Ke, 1999; Wang et al., 2012), sea-level rise, and increasing storminess (e.g., Feng & Tsimplis, 2014; Möller et al., 2014). This combination of anthropogenic and natural factors (Day et al., 2007) is adding unprecedented pressure on tidal mudflats (Abuodha & Woodroffe, 2006; Bird, 1986; Chen & Chen, 2002; Gornitz et al., 1994), which may lead to their eventual disappearance in some regions of the world.

The magnitude of bed erosion–accretion occurring within a tidal cycle has a critical influence on ecosystems. For example, short-term sediment dynamics are known to control benthic communities (Hall, 1994; Jumars & Nowell, 1984; Miller & Sternberg, 1988; Tuck et al., 2000; Ysebaert et al., 2003; Zajac & Whitlatch, 2001), especially via extreme erosional or depositional events (Tuck et al., 2000). As such, excessive bed erosion–accretion can result in total loss of a marine benthic community, requiring subsequent recolonization

(Miller et al., 2002). Hence, it is important to have an improved understanding of erosion–accretion dynamics on tidal mudflats.

Sediment erosion, deposition, transport, and mixing processes are controlled strongly by non-linear interactions between tidal currents and waves (Herman et al., 2001; Houwing, 1999; Janssen-Stelder, 2000; MacVean & Lacy, 2014; Ni et al., 2014; Shi et al., 2012; Turner et al., 1997; Wang et al., 2006). However, it remains poorly understood as to how these interactions cause morphological changes within an entire tidal cycle (Pratolongo et al., 2010; Widdows et al., 2008). This shortcoming is due mainly to a lack of field data on bed-level change and sediment dynamic processes during very shallow-water stages (VSWS, water depth < 0.2 m), when it is difficult to perform measurements so close to the mudflat bottom. Despite their significant influence on the morphological evolution of tidal mudflats, short-term sediment dynamics during VSWS are poorly documented, and few studies have quantitatively explored the magnitude of bed-level changes during VSWS. As a result, there is a lack of knowledge on the errors in predictive models of bed-level change when water is very shallow. In addition, the maximum changes in bed-level within an entire tidal cycle are likely to occur when the water depth is less than 0.2 m (Fagherazzi & Mariotti, 2012), because such stages are generally characterized by pulses of current velocity, potential breaking wave impacts, and high suspended sediment concentrations (SSCs) (Zhang et al., 2016). These hydrodynamics are likely to result in strong sediment re-suspension, as well as high erosional and depositional fluxes associated with horizontal advection, even though the VSWS commonly last for only a few minutes or even a few seconds (Gao, 2010). As a result, predictive models of bed-level change that do not directly account for the sediment dynamics that occur during very shallow conditions may underrepresent the true magnitude of change. Therefore, these short-term erosional and accretional processes should be examined to improve the accuracy of predictions of morphological change in tidal mudflats.

The aim of this study is to identify the morphological changes during VSWS and provide an improved understanding of the fundamental question of whether erosion and accretion processes of VSWS in intertidal mudflats play a significant role in the morphological changes observed during a tidal cycle. To achieve this, we present field observations of changes in water depth, current velocity, bed-level elevation, and near-bed SSC through numerous tidal cycles on the Wanggang mudflat on the Jiangsu coast, China. The field measurements were combined with theoretical models of current–wave sediment transport, and a time-series of bed-level changes within an entire tidal cycle is calculated and used to explore the importance of erosion and accretion during VSWS in terms of overall morphological change within an entire tidal cycle. In doing this, we highlight the effects of bed-level changes during very shallow conditions on mudflat morphodynamics and benthic habitat availability.

2. Study Area

The field study was carried out on Wanggang mudflat on the Jiangsu coast, China, between the Yangtze River estuary and the abandoned Yellow River mouth (Figure 1). This mudflat is composed of fine-grained sediments lying on a very gentle slope (mean gradient 0.018%–0.022%) and extends for several kilometers seaward (Wang & Ke, 1997; Zhu et al., 1986). Surficial sediment grains coarsen seaward, with the upper intertidal area characterized by silt (8–63 μm) and the lower area by very fine sand (63–125 μm) (Wang et al., 2012). The median grain size (D_{50}) of surface sediments in the middle and lower parts of the intertidal flat ranged from 68.1 to 75.7 μm (Table 1), made up of 55.0%–64.4% sand, 32.0%–39.2% silt, and 3.6%–7.3% clay (Table 1). Vegetation is absent from the intertidal range. The mudflat is very flat, with no conspicuous tidal creek system or gullies. The area has small ripples near the observation site (Figure 1b). The mean annual wind speed is 4–5 m/s, as recorded at Dafeng Harbor, ~5 km north of Wanggang mudflat.

The coastal hydrodynamics are influenced by a large radial sand-ridge system in the southern Yellow Sea off the Jiangsu coast, and characterized by a radial current field and high turbidity due to abundant sediment supply from the Yangtze River estuary and the abandoned Yellow River mouth (e.g., Shi et al., 2016; Wang, 2002; Zhang et al., 2016).

The semidiurnal macro-tidal regime has an average tidal range of 3.9–5.5 m (e.g., Ren, 1986; Yang et al., 2016a, 2016b), with higher tidally averaged current velocity in the middle intertidal mudflat than in the upper mudflat (Wang et al., 2012). During VSWS, the velocity maximum may last a few minutes or, in some rare cases, just several seconds, but these periods are characterized by large concentrations of suspended sediment that are commonly >1 kg/m^3 (Gao, 2010).
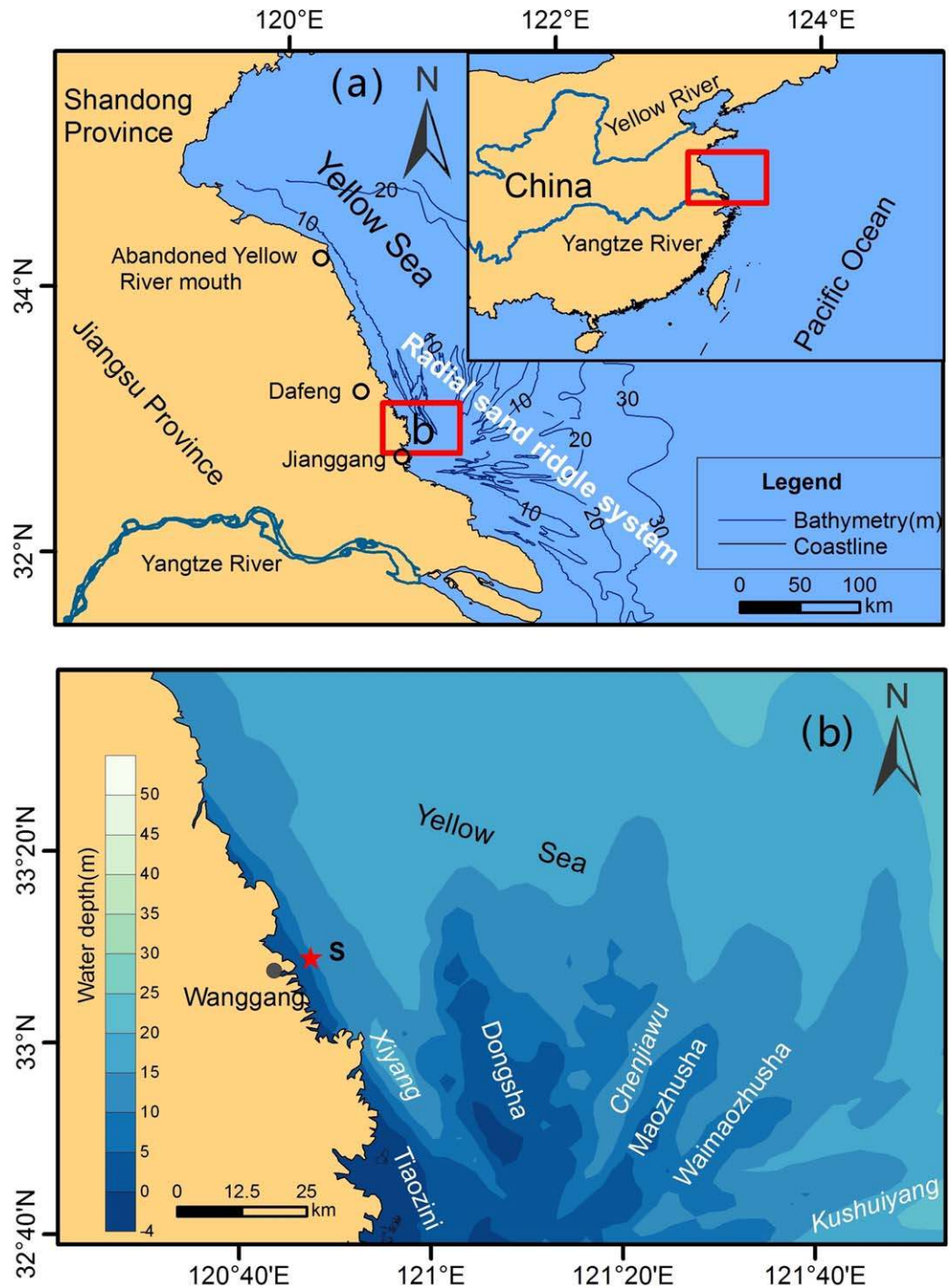
Figure 1. (a) Location of the studied area and (b) enlarged view of the area indicated by the red five-pointed star, showing the location of the observation site S on the Wanggang mudflat, Jiangsu coast, China.

3. Materials and Methods

3.1. Data Collection

The field survey was conducted between 27 April and 2 May 2013 on the Wanggang mudflat (Figure 1b). Time-series of water depth, wave height, turbidity, near-bed velocity, and bed-level change were acquired by instruments attached to a tripod (Figure 2). The tripod legs were pushed 1.5 m deep into the sediment

Table 1

Results of Bottom Sediment Grain-Size Analysis, Component Analysis, and Ripple Measurements at the Study Site During the Field Measurements (27 April to 2 May 2013)

Date (time)	D_{50} (μm)	Sediment component content (%)			Ripples (cm)	
		Sand	Silt	Clay	λ	η
Apr.27 (16:00)	71.5	55.04	37.64	7.32	5.5	1.8
Apr.28 (10:00)	68.1	56.62	39.16	4.22	6.3	1.9
Apr.29 (10:00)	71.8	59.93	35.29	4.78	7.4	2.3
Apr.30 (10:00)	75.7	64.39	32.02	3.59	6.2	1.5

Note. D_{50} denotes the median grain size of the sediments, η is the ripple height, and λ is the ripple wavelength.

to ensure stability during field measurements (Figure 2). During all field measurements, wind speed and direction were recorded every minute at Dafeng Harbor (Figure 1a), ∼5 km from the observation site.

A SBE 26plus SEAGAUGE (wave–tide recorder; Sea-Bird Electronics, USA) was deployed to measure water depth. The instrument was fastened to the tripod at a height of 0.1 m above the surface sediments and water-level fluctuations were recorded at 4 Hz, over every 256 s burst period, generating a total of 1,024 measurements per ensemble. The water depths and wave parameters (significant wave height and mean period) were then calculated from the zeroth moment and the second moment of the spectrum.

Turbidity was measured using an optical backscatter sensor (OBS-3A, self-recording turbidity–temperature monitoring instrument). The OBS-3A probe was attached to the tripod at a height of 0.15 m above the bottom sediment, facing outward (Figure 2). The OBS-3A measurements were calibrated using water samples retrieved during field measurements to derive SSC values. Water samples were collected from a small boat, using a custom-made sampler (volume 600 mL) positioned at the same height as the OBS-3A to calibrate *in situ* the turbidities measured by OBS-3A.

A 6 MHz Nortek acoustic Doppler velocimeter (ADV) was used to record near-bed velocities and bed-level changes. The ADV probe was attached to the tripod and deployed 0.2 m above the seabed, pointing downward (Figure 2), and thus measurements of velocity could only be made when the water depth exceeded 0.2 m. To estimate bed-level changes when the probe was submerged (water depth > 0.2 m), the ADV was set up in burst mode at 10 min intervals (sampling time) to record the distance between the probe and the surface sediment at the beginning of each sampling period (burst) with a vertical accuracy of ±1 mm
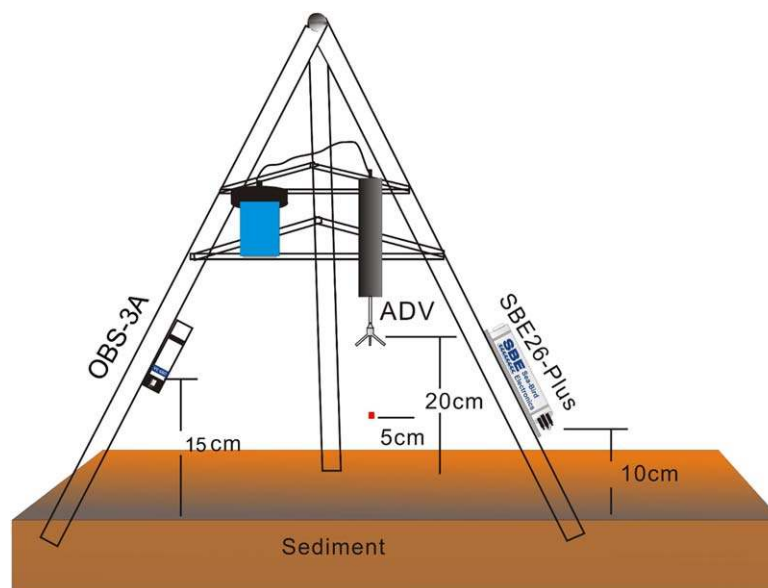

Figure 2. Schematic of the tripod and instrumentation deployed at the observation site during field measurements. ADV: Acoustic Doppler Velocimeter; SBE 26-plus: SBE 26-plus SEAGAUGE wave–tide recorder (Sea-Bird Electronics, USA); OBS-3A: optical backscattering sensor.

(Andersen et al., 2007; Salehi & Strom, 2012; Shi et al., 2015). Laboratory experiments have shown that bed-level changes measured in this way are accurate when the changes detected by the ADV are more than 1 mm (Salehi & Strom, 2012). For water depths of >0.2 m (ADV probe submerged), burst-based bed-level changes (Δz_b) were estimated as follows:

$$\Delta z_b = d_{b+1} - d_b \tag{1}$$

where d_b is the vertical distance recorded from the ADV probe to the bottom at the beginning of burst b, and d_{b+1} is the vertical distance recorded from the ADV probe to the bottom at the beginning of burst $b + 1$. Positive values of Δz_b indicate erosion between bursts b and $b + 1$ (with a time interval of 10 min), and negative values indicate deposition (Salehi and Strom, 2012; Shi et al., 2015; Wang et al., 2014). Index b accounts for the position within the time-series of the measured elevations.

For VSWS, the magnitudes of bed-level changes were estimated as the difference in bed elevation between the last measurement of the ebb period in the i-th tide and the first measurement during the flood period in the following $(i + 1)$-th tide. The bed-level change ($\Delta z_{i-(i+1)}$) during VSWS was estimated as follows:

$$\Delta z_{i-(i+1)} = d_{i+1} - d_i \tag{2}$$

where d_i is the vertical distance recorded from the ADV probe to the bottom at the beginning of the last burst during the ebb period in tide i, and d_{i+1} is the vertical distance recorded from the ADV probe to the mudflat bottom at the beginning of the first burst during the flood period in tide $i + 1$. Subscript i indicates the i-th tide series. In addition, we accurately recorded the time at which the water depth was zero for each tide, from a boat anchored close to the observation site, and when the instrument could not measure water level (i.e., when the ADV instrument was emergent).

There is a significant relationship between mean current velocity ($\bar{U}$) and ripple migration rate (U_r) (Grant, 1983), and thus estimates of U_r during submergence of the ADV probe (water depths > 0.2 m) were made using the ADV data and the following equation (Grant, 1983):

$$\log U_r = 1.935 \ \log \bar{U} - 4.935 \tag{3}$$

3.2. Estimation of Bed Shear Stress for the Stage of Water Depth > 0.2 m

For the observed conditions, the shear stress due to waves (τ_w) was estimated according to van Rijn (1993):

$$\tau_w = \frac{1}{2} \rho_w f_{wr} \ \hat{U}_\delta^2 \tag{4}$$

where ρ_w is seawater density (1,030 kg/m^3). The wave orbital velocity ($\hat{U}_\delta$) at the edge of the wave boundary layer is given by

$$\hat{U}_\delta = \omega \ \hat{A}_\delta \tag{5}$$

where ω (= $2\pi/T$) is the angular velocity and $\hat{A}_\delta$ is the peak value of the orbital excursion, given by

$$\hat{A}_\delta = \frac{H}{2\sinh\left(\frac{2\pi}{L} h\right)} \tag{6}$$

where H is significant wave height, h is water depth, L is the wavelength (= $(gT^2/2\pi)$ tanh$(2\pi h/L)$), g is gravitational acceleration (9.8 m/s^2), and T is the mean period. Following Soulsby (1997) method, $\hat{U}_\delta$ can be calculated directly from the input parameters H, T, h and g, via the quantity $Tn = (h/g)^{1/2}$.

Based on Soulsby (1997), the wave friction coefficient f_{wr} depends on the hydraulic regime, and can be expressed as

$$f_{wr} = \begin{cases} 2Re_w^{-0.5} \ , \ Re_w \leq 10^5 \, (\text{laminar}) \\ 0.0521 Re_w^{-0.187} \ , \ Re_w > 10^5 \, (\text{smooth turbulent}) \\ 0.237 \ r^{-0.52}, \ (\text{rough turbulent}) \end{cases} \tag{7}$$

where $Re_w \left(= \frac{\hat{U}_\delta \ A_\delta}{\nu} \right)$ is the wave Reynolds number and r ($= \frac{A_\delta}{k_s}$) is the relative roughness. Based on the recommendations of Davies and Thorne (2005) and Shi et al. (2012, 2016), the equivalent bed roughness was

estimated from $k_s = 25\ \eta^2/\lambda$ (Davies & Thorne, 2005), where η is the ripple height and λ is the ripple wavelength. The ripple heights and wavelengths, measured by a ruler during bed exposure after ebb, ranged from 1.5 to 2.3 cm and 5.5 to 7.4 cm, respectively (Table 1).

The three-dimensional (3D) velocities derived from the ADV measurements were used to estimate the shear stress due to currents (τ_c). The mean and turbulent flow velocities were first derived from these measurements using a Reynolds decomposition:

$$u = \bar{u} + u' \tag{8}$$

$$v = \bar{v} + v' \tag{9}$$

$$w = \bar{w} + w' \tag{10}$$

where u, v, and w are the measured instantaneous velocities in each of the three directions, $\bar{u}, \bar{v}$, and $\bar{w}$ denote the mean velocities, and u', v', and w' are the turbulent fluctuating velocities. The turbulent kinetic energy (TKE) was then estimated and used to calculate the shear stress due to currents (τ_c, N/m^2), according to Andersen et al. (2007) and Shi et al. (2015) as follows:

$$TKE = (u'^2 + v'^2 + w'^2)/2 \tag{11}$$

$$\tau_c = C_1\ TKE \tag{12}$$

where C_1 is a constant (0.19; Kim et al., 2000; Pope et al., 2006; Stapleton & Huntley, 1995). Although this TKE method for estimation of τ_c mentioned above has been applied widely in the published literatures (e.g., Biron et al., 2004; Bowden & Fairbairn, 1956; Joshi et al., 2017; Soulsby & Dyer, 1981; Williams et al., 1999), it is noteworthy that the calculation of τ_c using equations (11) and (12) will be contaminated by wave action when waves are measurable at the sampling volume.

Another method of estimating τ_c is derived from a modified TKE-method (TKE$_w$) (Huntley & Hazen, 1988), based on vertical turbulent kinetic energy alone:

$$\tau_c = C_2 w'^2 \tag{13}$$

where C_2 is a constant of 0.9, as recommended by Kim et al. (2000).

The bed shear stress due to combined current–wave action τ_{cw} was calculated using the van Rijn (1993) model ($\tau_{cw-van\ Rijn}$), Soulsby (1995) model ($\tau_{cw-Soulsby}$), and Grant and Madsen (1979) model ($\tau_{cw-Grant-Madsen}$) as follows:

$$|\tau_{cw-van\ Rijn}| = \tau_c + |\tau_w| \tag{14}$$

$$\tau_{cw-Soulsby} = \tau_c \left[1 + 1.2 \left(\frac{\tau_w}{\tau_c + \tau_w} \right)^{3.2} \right] \tag{15}$$

$$\tau_{cw-Grant-Madsen} = \left[(\tau_w + \tau_c |cos\ \varphi_{cw}|)^2 + (\tau_c |sin\ \varphi_{cw}|)^2 \right]^{1/2} \tag{16}$$

where τ_w and τ_c are the bed shear stress due to waves and currents (N/m^2), respectively, and φ_{cw}(°) is the angle between the current direction and wave direction. In the van Rijn (1993) model, τ_c is positive when the wave direction is the same as the current direction, and negative when they are in opposing directions. To determinate the wave direction, we combine horizontal velocities and pressure data from the ADV using a standard PUV method (available at http://www.nortekusa.com/usa/knowledge-center/table-of-contents/waves), and some MATLAB tools in the Nortek web page that can compute wave directional spectra from data using Nortek Vector. These models have been widely employed in estimating bed shear stress due to current–wave interaction (e.g., Feddersen et al., 2003; Keen & Glenn, 2002; Lyne et al., 1990; Mellor, 2002; Shi et al., 2012; Styles & Glenn, 2002; and reference therein).

3.3. Prediction of Bed-Level Changes

The rates of variation in bed-level elevation (Δz) were modeled using the three different shear-stress equations (equations (14–16)), and were directly related to the erosional (E) and depositional (D) fluxes (Winterwerp & van Kesteren, 2004) as follows:
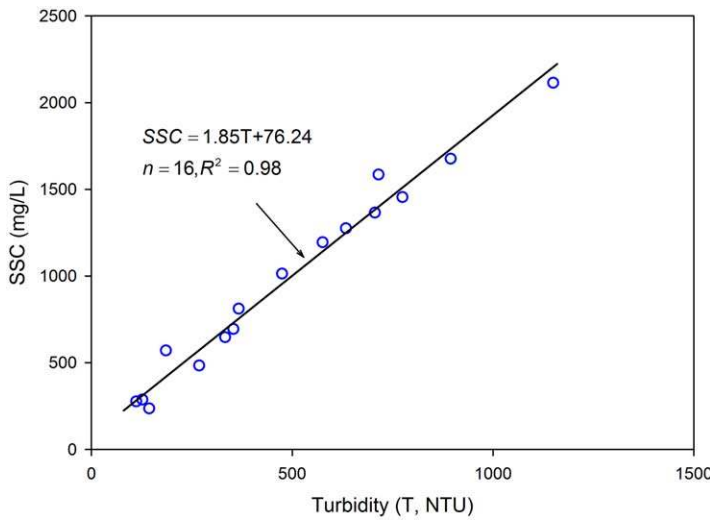
Figure 3. Regression relationship between SSC (mg/L, suspended sediment concentration) and turbidity (T with turbidity units in NTU) of corresponding in situ water samples recorded by OBS-3A at observation site S. n is the number of water samples and R^2 is the correlation coefficient.

$$\Delta z = \int_0^t \frac{D-E}{\rho_{dry}} dt \tag{17}$$

where D is the depositional flux (mass deposition per unit area per unit time in kg/m^2/s) related to near-bed SSC and the settling velocity of suspended particles, t is the measurement interval (s), and E is the erosional flux (kg/m^2/s). According to Whitehouse et al. (2000) and Winterwerp and van Kesteren (2004), D can be estimated as

$$D = (SSC)\, w_{50} \tag{18}$$

where SSC is the near-bed suspended sediment concentration measured by OBS-3A (kg/m^3). To obtain near-bed SSCs in the field, the relationship between the SSC of water samples and turbidities needs to be established by a calibration equation. In this study, there was a strong correlation between the SSCs of water samples and corresponding turbidities (Figure 3). Thus, all *in situ* measured turbidities can be converted to corresponding SSCs using the calibration equation (SSC = 1.85 T + 76.24; T = turbidity) provided by Figure 3. w_{50} is the settling velocity of the median grain size, and was derived from the Soulsby formula (Soulsby, 1997), which is widely used in studies of the settling velocity of fine sediment flocs in suspension (i.e., Floyd et al., 2016; Soulsby, 2000; Spearman & Manning, 2017), and can be expressed as follows (Whitehouse et al., 2000):

$$w_{50} = \frac{v}{d_e}\left\{ \left(10.36^2 + 1.049\ (1-C_f)^{4.7}D_*^3\right)^{\frac{1}{2}} - 10.36 \right\} \tag{19}$$

$$d_e = \left(\frac{SSC}{\rho_s}\right)^{\frac{m}{2}} \left[\frac{19.8\ \rho\ v\ \rho_s^m\ k}{g(\rho_e - \rho)}\right]^{\frac{1}{2}} \tag{20}$$

$$D_* = d_e\left[\frac{g(\rho_e - \rho)}{\rho\ v^2}\right]^{\frac{1}{3}} \tag{21}$$

$$C_f = \frac{(\rho_s - \rho)(SSC)}{(\rho_e - \rho)\ \rho_s} \tag{22}$$

where the dimensionless floc diameter d_e is the effective diameter of a floc; g is gravitational acceleration (9.8 m/s^2); D_* is a dimensionless grain diameter; ρ_s is the mineral density of the grains (2,650 kg/m^3); ρ is water density (1,030 kg/m^3); ρ_e is the effective density of flocs (1,078 kg/m^3; $\rho_e = \rho + C_{in}\ (\rho_s - \rho)$, in which C_{in} is the internal volume concentration of grains inside a floc, and values of C_{in} are found to range from ca. 0.025 to 0.04, with C_{in} = 0.03 used as a default value); v is the kinematic viscosity (1.36 × 10^{-6} m^2/s), and m and k are best-fit coefficients. To determine these two coefficients, we performed a sensitivity analysis on the coefficient values in equation (20) (Figure 4), by applying all possible combinations of m and k values into equations (17) and (19–22). Thus, values of m and k were obtained by selecting the one combination of values that best matched the predicted change in bed-level with the change measured by ADV during Tide 1. This analysis gave m and k values of 0.002 and 1.5 in equation (20), respectively. Consequently, w_{50} was 3 × 10^{-3} m/s, which is the same order of magnitude as previously published values for fine-grained suspended sediments (e.g., Whitehouse et al., 2000; Winterwerp & van Kesteren, 2004).

The erosional flux was estimated according to Winterwerp and van Kesteren (2004):

$$E_{model\ 1} = M_E(\tau_{cw-van\,Rijn} - \tau_{ce})\rho_{dry} \qquad \text{for}\quad \tau_{cw-van\,Rijn} > \tau_{ce} \tag{23}$$

$$E_{model\ 2} = M_E(\tau_{cw-Soulsby} - \tau_{ce})\rho_{dry} \qquad \text{for}\quad \tau_{cw-Soulsby} > \tau_{ce} \tag{24}$$

$$E_{model\ 3} = M_E(\tau_{cw-Grant-Madsen} - \tau_{ce})\rho_{dry} \qquad \text{for}\quad \tau_{cw-Grant-Madsen} > \tau_{ce} \tag{25}$$

where ρ_{dry} is the dry sediment density (kg/m^3). Given that sediments on the Wanggang mudflat originate from the Yangtze River, the dry density used for this surface sediment (ρ_{dry}) was 1,300 kg/m^3 based on the

recommendation of Yang et al. (2007). M_E is the erodibility parameter (m/Pa/s), and the applied value of M_E in this study was 2.19×10^{-6} m/Pa/s, which is applicable for the neighboring intertidal mudflat at the Yangtze delta front based on Shi et al. (2014), and is also of the same order of magnitude as a large number of published results (e.g., Shi et al., 2017; Winterwerp & van Kesteren, 2004). τ_{ce} is the critical shear stress for the erosion of bottom sediments (N/m^2). For fine sediments with high water content, there is a close correlation between τ_{ce} and water content. Thus, τ_{ce} (0.11 N/m^2) was estimated based on a formula derived from the experimental results of Taki (2001) that are applicable to fine sediments (typically less than several tens of microns) and relatively high water contents (see Appendix A). Due to the reliance of both models on estimates of τ_{cw} derived from ADV data, bed-level changes were only modeled when the water depth was > 0.2 m.

3.4. Comparison of Predicted and Measured Bed-Level Changes

Comparisons of the modeled and measured time-series of bed-level changes were made in two different situations to explore the importance of very shallow-water conditions on these changes: (i) considering only the probe submersion period (i.e., water depths > 0.2 m) (equations (14)–(16)); and (ii) considering the entire tidal cycle. For (ii), the bed-level changes for VSWS were estimated using equation (2), and the time-series of bed-level changes for the rest of the cycle was modeled using equation (17). Thus, if the sediment dynamics during the VSWS have an important influence on the total bed-level change, one would expect a difference between (i) and (ii).

3.5. Comparison of Measurements and Modeled Results

To quantify the difference between the time-series of modeled and measured bed-level change, we used the index of agreement (I_{ag}) proposed by Willmott et al. (1985), defined as

$$I_{ag} = 1 - \frac{\sum_{i=1}^{N}(P_i - M_i)}{\sum_{i=1}^{N}[|P_i - \bar{M}| + |M_i - \bar{M}|]} \tag{26}$$

where P_i and M_i are the i-th time-series of modeled and measured values of bed-level changes obtained from equation (17) and the ADV data, respectively, and $\bar{M}$ is the mean of the measured time-series of bed-level changes (ADV data). The index I_{ag} varies between 0 and 1; 0 denotes complete disagreement and 1 indicates perfect agreement between the modeled and measured data.

The Brier Skill Score (BSS) is one of the most suitable methods for assessing morphological predictions (Sutherland et al., 2004), because it ignores model predictions where there is little or no change. One disadvantage of the score is that it heavily penalizes small predicted changes when the measurement reveals no change. The score is defined as

$$BSS = 1 - \frac{BS}{BS_c} \tag{27}$$

$$BS = \frac{1}{n}\sum_{i=1}^{n}(P_i - M_i)^2 \tag{28}$$

$$BS_c = \frac{1}{n}\sum_{i=1}^{n}(P_c - M_i)^2 \tag{29}$$

$$P_c = \frac{1}{n}\sum_{i=1}^{n}M_i \tag{30}$$

where BS is the Brier score and BS_c is the Brier score of the reference probability forecast, which is commonly known as the probability of event occurrence from climatology. The P_c is an average climatology and P_i and M_i are the i-th time-series of modeled and measured values of bed-level changes, respectively. A BSS of 1.0 indicates a perfect probability forecast, whereas a BSS of 0.0 should indicate the skill of the reference forecast, and a BSS < 0.0 indicates that the mean of the measured values is a better predictor than that produced by a given model.
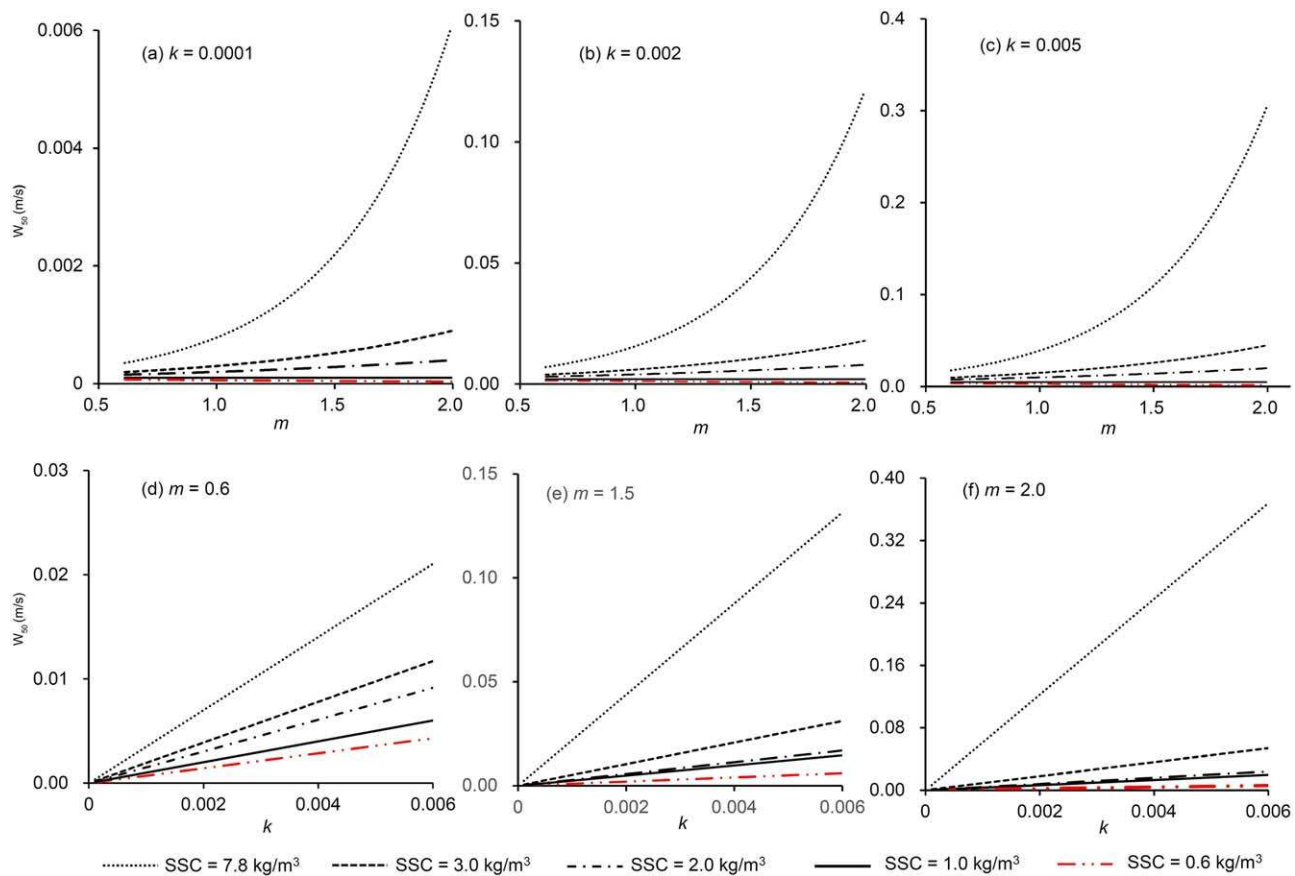
Figure 4. Sensitivity analysis of the model coefficients m and k in equations (19)–(22). The subplots a–c show that 1000 numbers of m between 0.5 and 2.0 were chosen randomly, and then all groups that matched m with k (0.0001, 0.002, and 0.005, respectively) were input to equations (19)–(22). The subplots d–f show that 1000 numbers of k between 0.0001 and 0.006 were chosen randomly, and then all groups that matched k with m (0.6, 1.5, and 2.0, respectively) were input into equations (19)–(22).

4. Results

4.1. Wind, Wave Parameters, and Currents

From Tide 1 to Tide 3, the wind speed during the flood tide was smaller than that during the ebb, and the wind prevailed in a southeasterly direction (133° to 168°; hourly data shown in Figure 5b). From Tide 4 to Tide 6, the wind speed during the flood stage was greater than that during the ebb stage. This was particularly the case at the beginning of Tide 4, when the wind speed reached up to 13.6 m/s (Figure 5b) and the wind direction switched from north (Tide 4) to east (Tide 5). Tidally averaged wind speed during Tides 5–9 was less than that during Tides 1–3.

The tidally averaged and maximum significant wave heights during Tide 4 were 0.17 and 0.38 m, respectively, much greater than during Tides 1–3 and 5–9 (Figure 6b). The time-series of current velocity during Tides 1–3 and 5–9 showed northward alongshore velocities rotating clockwise, whereas during Tide 4 the peak velocity tended to be in the initial flood stage, possibly because of the stronger northerly wind; subsequently, there was a strong alongshore velocity rotating clockwise (Figure 5c). The maximum alongshore velocities in all nine tidal cycles occurred during slack waters, and the average current velocity was higher during the ebb tide than the flood tide (Figure 5c).

4.2. Power Spectrum of Velocities and Waves

Power spectrum analysis of the velocity data showed that the power density in the low-frequency range (0.02–0.03 Hz) was at least one order of magnitude higher than that in the high-frequency range (0.24–0.34 Hz) during Tides 2, 3, 4, and 6 (Figures 7a–7d and 7f). At the flood stage of Tide 4, however, there was only a small period of large wave heights (>0.3 m), and the power in the low-frequency range (0.02–0.03 Hz)
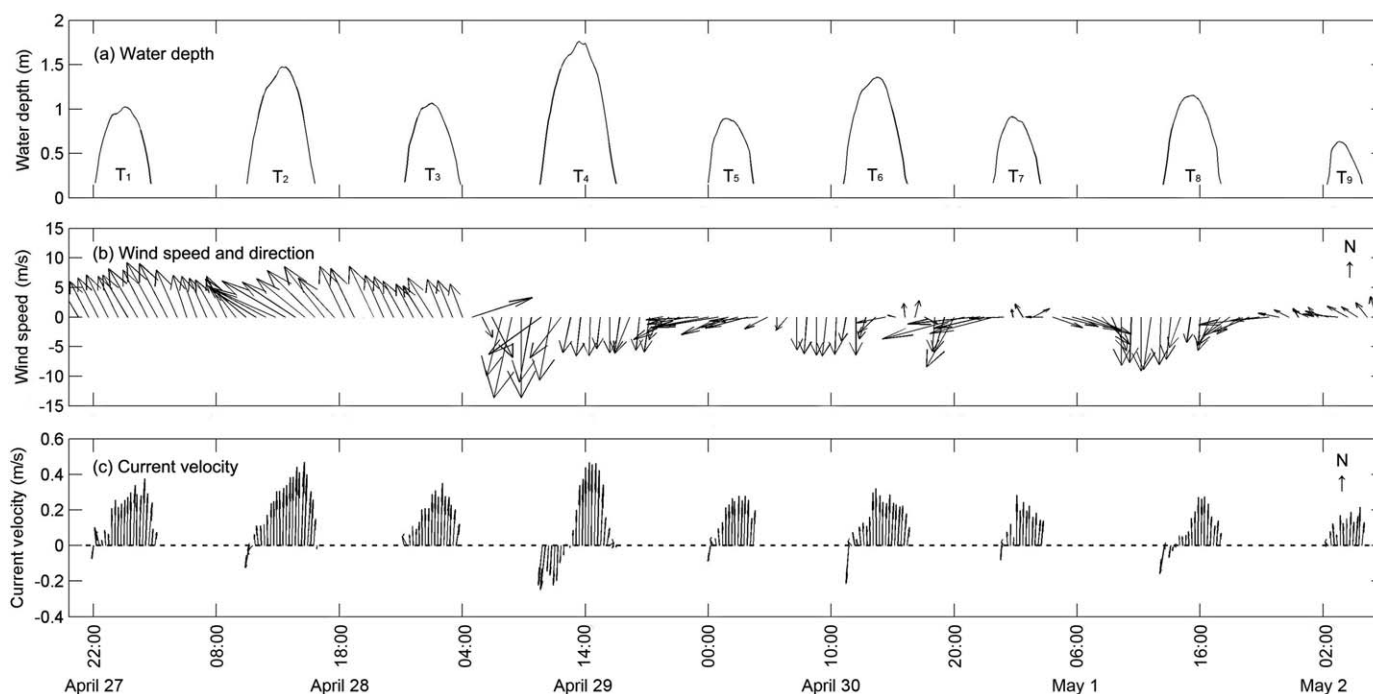
Figure 5. Time-series of (a) water depth, (b) wind speed and direction, and (c) current velocity during the field measurements (27 April to 2 May 2013). The wind data were recorded every hour at the Wanggang Gauging station, which is located to the northeast of the study site. The vector direction of the wind/current is based on the Darth coordinate, i.e., N (north) toward top and E (east) toward the right. Note: The vector direction of wind is direction from which the wind blows. Water depths of <0.2 m indicate that effective data recording stopped because the instrument sensors were exposed to air.

was comparable to that in the high-frequency range (0.24–0.4 Hz) (Figure 7e). A large peak in the spectrum was evident at a frequency around 0.03 Hz, and a small peak at around 0.3 Hz (Figures 7a–7d and 7f). These peaks show that the near-bed velocity is not significantly affected by wave motions under calm weather condition. In contrast, at the beginning of the flood stage of Tide 4 (windy weather conditions), there was a peak value at 0.27 Hz, and the power density was of a similar magnitude to the peak power density at around 0.03 Hz (Figure 7e), showing that the TKE was significantly affected by wave action under windy weather conditions (i.e., relatively large wave heights). The energy spectra of waves derived from combined wave orbital and turbulent velocities in the east, north, and up directions showed no major peaks. The maximum value of wave power density was 0.04 m^2/Hz, which occurred at the flood stage of Tide 4 (Figure 8). This result also suggests that during an earlier period in Tide 4, near-bed turbulent velocities were affected by wave action.

4.3. Bed Shear Stress

Tidally averaged values of τ_c were higher than τ_w during Tides 1–3 and 5–9 (Figures 6c and 6d), but τ_w was dominant in Tide 4 during the flood tide (Table 2), showing that currents dominated the hydrodynamics during Tides 1–3 and 5–9 and waves dominated during Tide 4. Results of estimating τ_{cw} using three models (Models 1, 2, and 3; Grant & Madsen, 1979; Soulsby, 1995; van Rijn, 1993) are shown in Figure. 6e and Table 2. Specifically, τ_{cw} based on the van Rijn (1993) model is greater than that based on the Grant and Madsen (1979) model, with τ_{cw} based on the Soulsby (1995) model being the lowest (Figures 6e and 9). Apart from Tide 4, the tidally averaged values of $\tau_{cw-van\ Rijn}$ were slightly higher than those of $\tau_{cw-Soulsby}$, but the values change similarly through time (Figure 6e). However, when focusing on τ_{cw} for just Tide 4, $\tau_{cw-van\ Rijn}$ is much higher than $\tau_{cw-Soulsby}$. The $\tau_{cw-van\ Rijn}$ values ranged from 0.01 to 0.45 N/m^2 (tide-averaged = 0.19 N/m^2), whereas the $\tau_{cw-Soulsby}$ values varied from 0.01 to 0.24 N/m^2 (tide-averaged = 0.11 N/m^2).

4.4. Suspended Sediment Concentrations

Although there was a small variability in SSCs (Figure 10b) within each submergence period during Tides 1–3 and 5–9, the peak value generally appeared at the beginning of the flood tide, as observed on other intertidal flats (Black, 1998; Li et al., 2007; Shi et al., 2014; Wang et al., 2012; Zhang et al., 2016). Wave periods
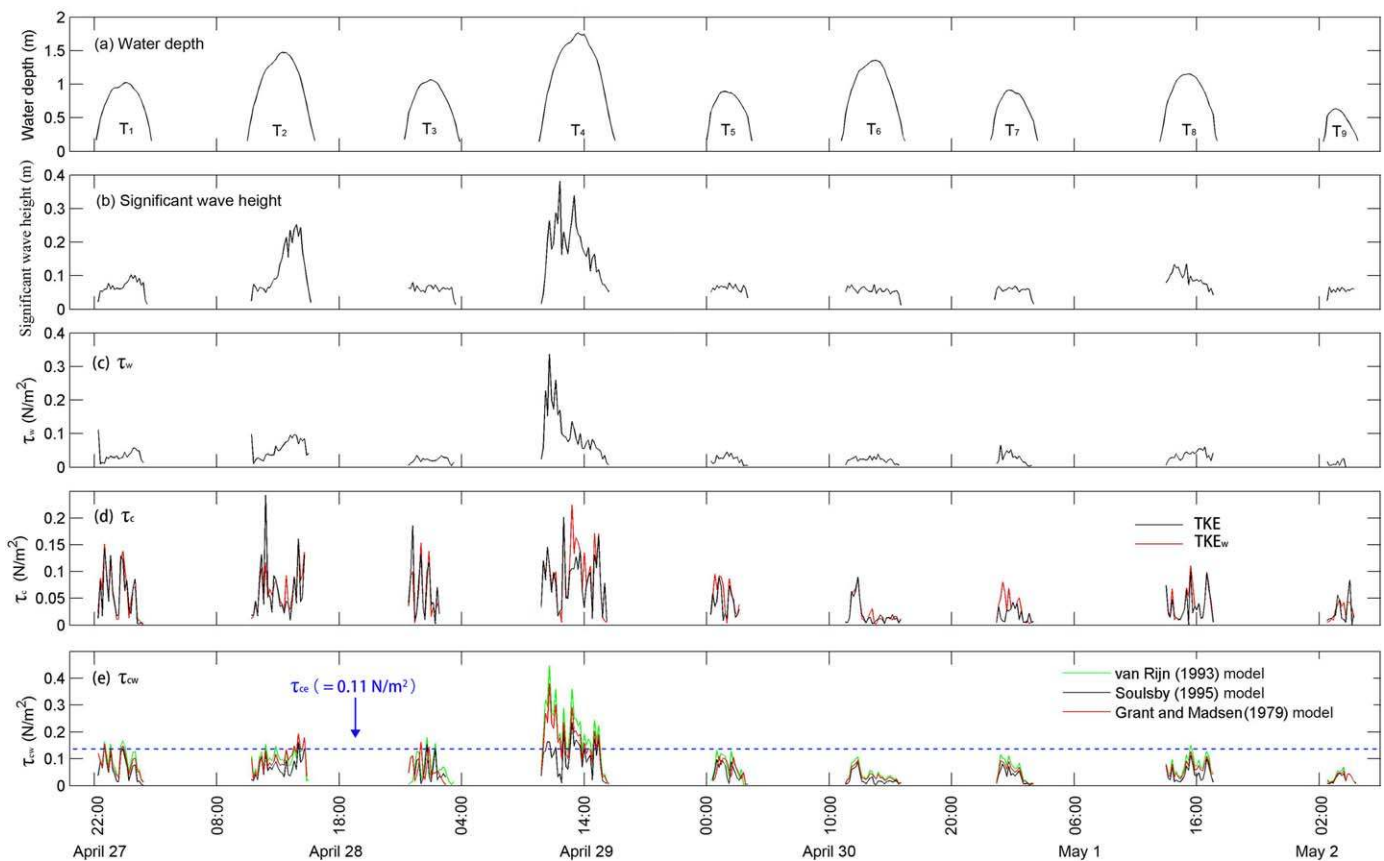
Figure 6. (a) Water depth, (b) wave height, (c) bed shear stresses due to currents (τ_c), (d) bed shear stresses due to waves (τ_w), and (e) bed shear stresses due to combined current–wave action (τ_{cw}) during the period of field measurements (27 April to 2 May 2013). TKE is based on the turbulent kinetic energy (i.e., turbulent fluctuations, equations (11) and (12)) (e.g., Pope et al., 2006; Salehi and Strom, 2012; Stapleton & Huntley, 1995), whereas TKEw is based on vertical turbulent kinetic energy alone (equation (13)) (e.g., Andersen et al., 2007; Huntley & Hazen, 1988; Kim et al., 2000). A water depth of <0.2 m indicates that effective data recording stopped because the instrument sensors were exposed to air.

derived from the wave–tide recorder ranged from 2 to 5 s during field measurements, suggesting that local winds lead to wind waves and all the dynamics are local because the waves are generated by local wind. The maximum and tidally averaged values of SSCs during Tide 4 were all higher than those during other tides, because strong erosion caused large volumes of bottom sediments to become re-suspended when local shear stress exceeded the critical shear stress for motion (i.e., $\tau_{cw} > \tau_{ce}$) (Figure 10f), resulting in a high near-bed SSC during the entire tidal cycle.

4.5. Erosional (*E*) and Depositional (*D*) Fluxes

The estimated values for $E_{model\ 1}$, $E_{model\ 2}$, $E_{model\ 3}$, $D_{calculated}$, $E_{observed}$, and $D_{observed}$ are shown in Figures 10c and 10d and Table 3. The $E_{observed}$ and $D_{observed}$ are the same order of magnitude as estimated E and D using equations (18) and (23–25) ($D_{calculated}$, $E_{model\ 1}$, $E_{model\ 2}$, and $E_{model\ 3}$) (Figures 10c and 10d). During Tides 1–3 and 5–9, the values of $E_{model\ 1}$, $E_{model\ 2}$, and $E_{model\ 3}$ were all close to zero, because $\tau_{cw-van\ Rijn}$, $\tau_{cw-Soulsby}$, and $\tau_{cw-Grant-Madsen}$ were less than τ_{ce} for the majority of the cycles (Figure 6e). D values ranged from 0.06×10^{-3} to 0.54×10^{-3} kg/m²/s and were typically higher than E values (Figures 10c and 10d; Table 3), suggesting that accretion was the dominant process during these tides. However, during Tide 4 erosional fluxes estimated using $\tau_{cw-van\ Rijn}$, $\tau_{cw-Soulsby}$, and $\tau_{cw-Grant-Madsen}$ were very different (Figure 10c). According to Model 1, the values of $E_{model\ 1}$ ranged from 0 to 22.50×10^{-3} kg/m²/s (average = 6.17×10^{-3} kg/m²/s), because $\tau_{cw-van\ Rijn}$ exceeded τ_{ce}, showing that erosion had occurred (Figure 6e and Table 3). According to Model 2, the values of $E_{model\ 2}$ were much smaller (0 to 8.84×10^{-3} kg/m²/s; average = 1.72×10^{-3} kg/m²/s), because the predicted values of $\tau_{cw-Soulsby}$ rarely exceeded τ_{ce}. Thus, Model 2 could not fully explain the observed erosion (Figure 10f and Table 3). According to Model 3, the values of $E_{model\ 3}$ (0
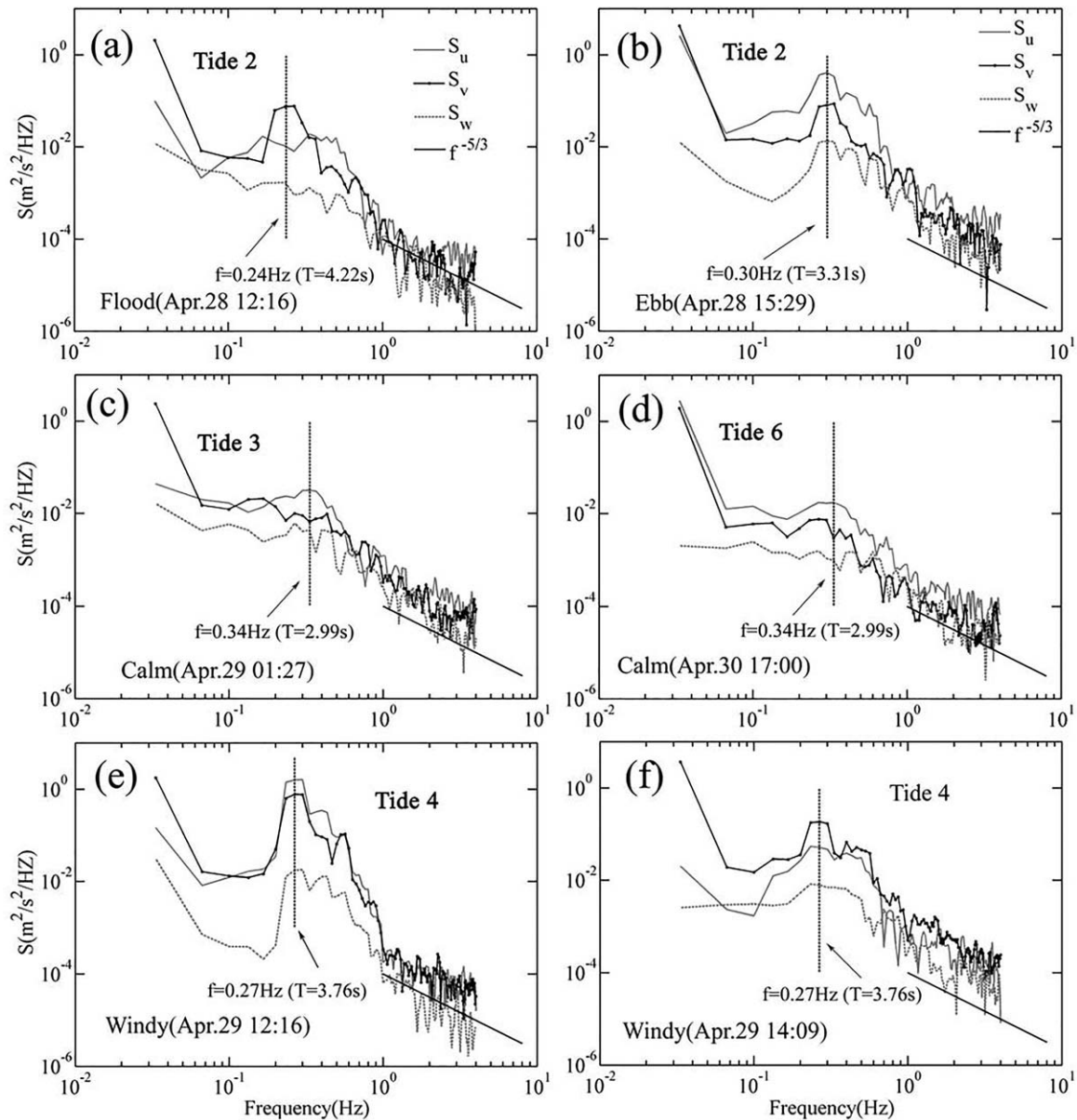
Figure 7. Power spectrum of the ADV velocities used to assess the significance of wave contamination during representative periods. In this study, representative periods included flood (a), ebb (b), calm (c, b), and windy (e, f).

to 18.25×10^{-3} kg/m^2/s; average $= 4.30 \times 10^{-3}$ kg/m^2/s) were between the two values given by $E_{model\ 1}$ and $E_{model\ 2}$.

4.6. Bed-Level Changes
4.6.1. Measured Values for the Entire Study Period
The distance from the ADV probe to the sediment surface decreased steadily from 190 mm at the beginning of the flood tide (the first burst during the submerged period in Tide 1) to 173 mm at the end of the ebb of Tide 3 (the last burst during the submerged period in Tide 3). This change indicates that the cumulative net accretion through Tides 1 to 3 resulted in a bed-level change of +17 mm (positive denotes accretion) (Figure 10f). Similarly, cumulative accretion through Tides 5 to 9 resulted in a net bed-level change of +28 mm. In contrast, during Tide 4 the distance from the probe to the bottom increased from 172 mm at the beginning of the flood in Tide 4 to 243 mm at the end of the submerged stage, indicating strong erosion (−70 mm; Figure 10f).
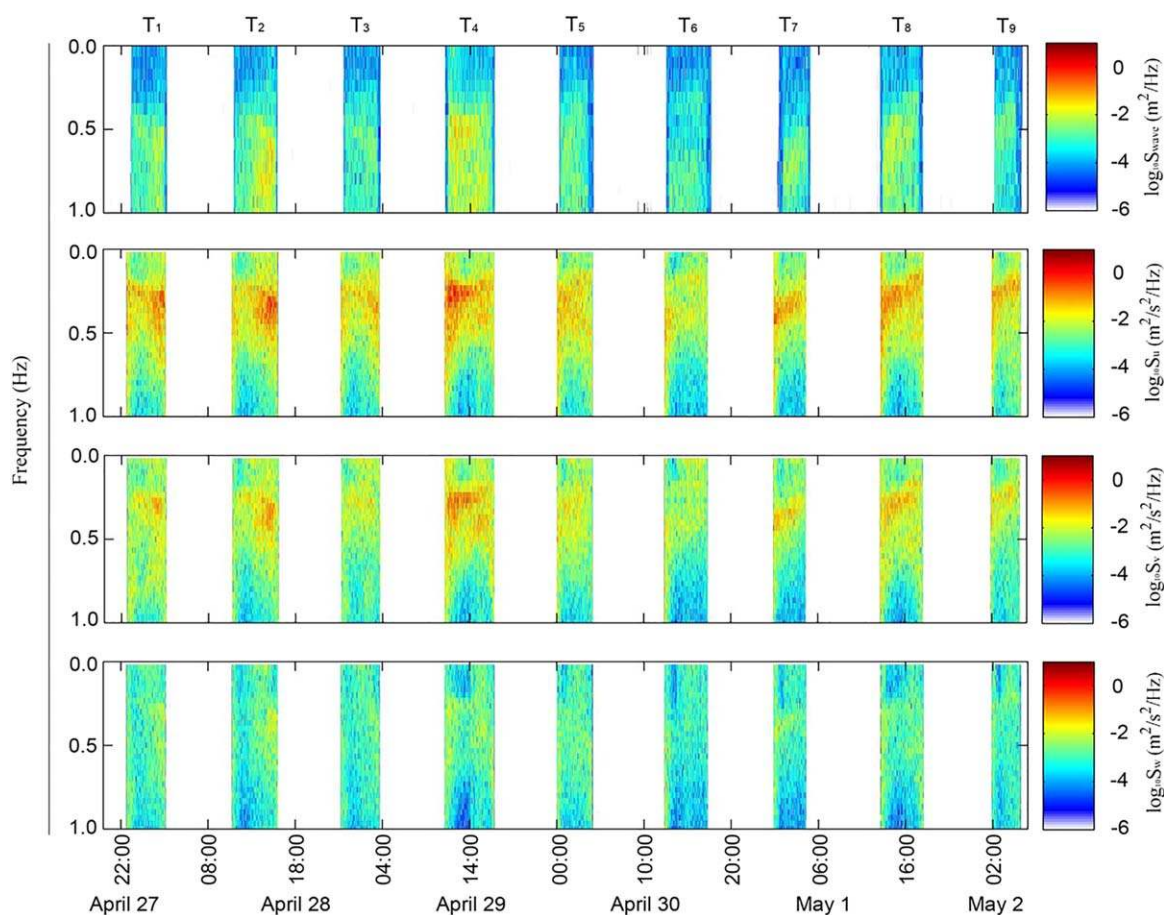
Figure 8. Time-series of the energy spectrum of waves (S_{wave}), and combined wave orbital and turbulent velocities in the east (S_u), north (S_v), and up (S_w) directions. T_1–T_9 indicate a series of tides during the field measurements.

4.6.2. Measured Values for Water Depths (h) of < 0.2 m and > 0.2 m

The bed-level changes during the VSWS (< 0.2 m) and submersion (> 0.2 m) stages were calculated using the time-series of bed-level elevation from the ADV (equations (1) and (2)) (Table 4). The total duration for water depths less than 0.2 m was 280 min, accounting for only 11% of the entire tidal cycles, but produced +14 mm of net accretion equaling 35% of the change in bed-level that was observed during the entire tidal cycle (Table 4). These two results reveal that morphodynamic changes during the VSWS were rapid and brief. To examine these changes in more detail, a comparison in changes in bed-level between phases of $h < 0.2$ m and $h > 0.2$ m for all tides is shown in Figure 11. The phase of $h < 0.2$ m (20 to 26 min) was dramatically shorter than the phase of $h > 0.2$ m (140 to 310 min per tide), equaling 15% of the entire tidal cycle (Figure 11). The average rate of change in bed-level during the accretion phase of $h < 0.2$ m (+17 mm/min) was dramatically greater than that during the accretion phase of $h > 0.2$ m (+2 mm/min). This average rate of change during the erosion phase of $h < 0.2$ m (–54 mm/min) was also greater than that during the erosion phase of $h > 0.2$ m (–17 mm/min) (Figure 11). These findings show that although the phase of $h < 0.2$ m only accounted for less than 15% of the entire tidal cycle, the rate of change in bed-level during the phase of $h < 0.2$ m was much higher than that during the phase of $h > 0.2$ m.

4.6.3. Tidally Cumulative Bed-Level Changes

During Tides 1–3 and 5–9, the three models (Models 1–3) performed similarly. Predicted tidally cumulative bed-level changes ranged from +1 to +3 mm, lower than the observed changes (+2 to +4 mm) (Figure 10e). For Tide 4, the predicted value for tidally cumulated bed-level change was −88 mm (Model 1), −13 mm (Model 2), and −57 mm (Model 3) (Figure 12). The predicted value of bed-level change using Model 3 is much closer to the measured −60 mm change (Figure 12), suggesting that Model 3 performed better. The reason for this may be that Model 3 is more accurate in describing wave dynamics than Model 2.

Table 2
Calculated Hydrodynamic Parameters, Including Bed Shear Stress Due to Currents (τ_c, N/m²), Waves (τ_w, N/m²), and Combined Current–Wave Action (τ_{cw}, N/m²) During the Total Period of Field Measurements

Tides	τ_w (N/m²)			τ_c (N/m²) for TKE			τ_{cw} (N/m²) for van Rijn (1993) model			τ_{cw} (N/m²) for Soulsby (1995) model			τ_{cw} (N/m²) for Grant and Madsen (1979) Model		
	Max	Min	Ave ± Std	Max	Min	Ave ± Std	Max	Min	Ave ± Std	Max	Min	Ave ± Std	Max	Min	Ave ± Std
1	0.11	0.01	0.04 ± 0.02	0.15	∼0	0.06 ± 0.05	0.17	0.02	0.09 ± 0.05	0.15	∼0	0.06 ± 0.04	0.15	0.01	0.08 ± 0.04
2	0.10	0.01	0.06 ± 0.03	0.16	0.01	0.07 ± 0.04	0.20	0.02	0.10 ± 0.04	0.16	0.02	0.07 ± 0.04	0.19	0.02	0.10 ± 0.04
3	0.03	∼0	0.02 ± 0.01	0.15	0.01	0.06 ± 0.05	0.18	∼0	0.06 ± 0.05	0.15	0.01	0.06 ± 0.04	0.16	∼0	0.06 ± 0.04
4	0.34	0.01	0.10 ± 0.07	0.22	0.01	0.09 ± 0.06	0.45	0.01	0.19 ± 0.10	0.24	0.01	0.11 ± 0.06	0.38	0.01	0.16 ± 0.09
5	0.04	∼0	0.02 ± 0.02	0.10	∼0	0.05 ± 0.05	0.13	∼0	0.07 ± 0.06	0.10	0.01	0.04 ± 0.05	0.11	∼0	0.06 ± 0.03
6	0.04	0.01	0.02 ± 0.01	0.09	∼0	0.02 ± 0.02	0.11	0.01	0.04 ± 0.03	0.09	∼0	0.02 ± 0.02	0.09	0.01	0.03 ± 0.02
7	0.19	∼0	0.03 ± 0.02	0.08	∼0	0.03 ± 0.02	0.12	0.01	0.06 ± 0.04	0.08	∼0	0.03 ± 0.02	0.09	∼0	0.05 ± 0.03
8	0.06	0.01	0.04 ± 0.04	0.11	0.01	0.04 ± 0.04	0.15	0.03	0.08 ± 0.08	0.11	0.01	0.05 ± 0.05	0.13	0.03	0.06 ± 0.03
9	0.03	∼0	0.01 ± 0.01	0.05	0.01	0.03 ± 0.02	0.07	0.01	0.04 ± 0.02	0.05	0.01	0.03 ± 0.02	0.06	0.01	0.03 ± 0.02

Note. ∼0 = very close to zero; Max = maximum value; Min = minimum value; Ave = average value; Std = standard deviation for an entire tidal cycle.

However, the reason for the large differences in modeled values during Tide 4 is that the value of τ_{cw} obtained by the van Rijn (1993), Soulsby (1995), and Grant and Madsen (1979) models differs (Figure 6e). That is, the τ_{cw} value decreases in the order of the *van Rijn* model, the *Grant–Madsen* model, and the *Soulsby* model (Figure 6e), resulting in differences in the predictions of tidally cumulative bed-level change during Tide 4 (Figure 10e).

4.6.4. Burst-Based Changes in Bed-Level (Δz_b)
Although there was a general trend of accretion in bed-level during Tides 1–3 and 5–9, and erosion during Tide 4 (Figure 10f), the burst-based changes in bed-level showed that the bed experienced frequent alternating periods of erosion and accretion (Figure 13). During Tides 1–3 and 5–9, Δz_b ranged from −6 (erosion) to +8 mm/10 min (accretion), and maximum changes in bed-level within a tidal cycle (∼0 to +1.28 cm) were less than the ripple height of the corresponding tidal cycle (1 to 2 cm) (Table 5). In contrast, during Tide 4, Δz_b ranged from −13 to +4 mm/10 min, and maximum changes in bed-level (–5.5 cm) were greater than ripple height (2.3 cm) (Table 5).

4.6.5. Agreement Between Modeled and Measured Cumulative Bed-Level Changes
Measured and modeled cumulative bed-level changes through the entire period (all tides from April 27 to May 2) are shown in Figure 14. Estimates obtained through Model 1 and Model 3 are always closer to the measured values, and the best agreement was obtained when the bed-level changes throughout the entire
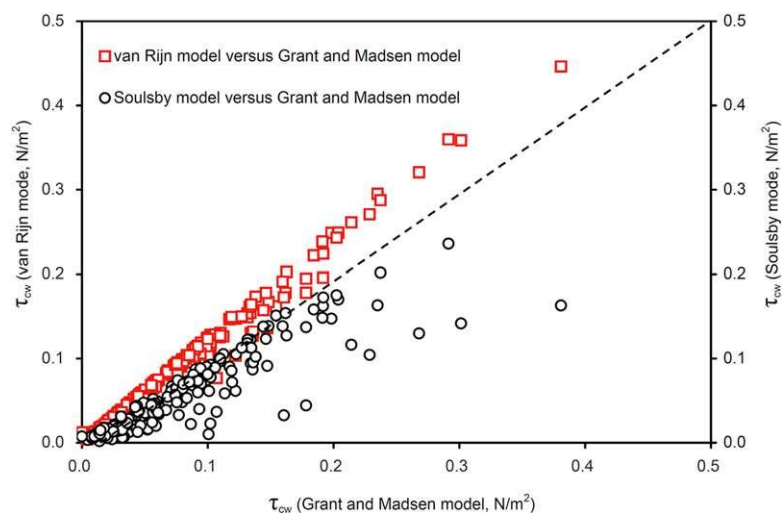

Figure 9. Comparison of τ_{cw} values derived from the models of Grant and Madsen (1979), Soulsby (1995) and van Rijn (1993). τ_{cw} is the bed shear stress due to combined current–wave action.
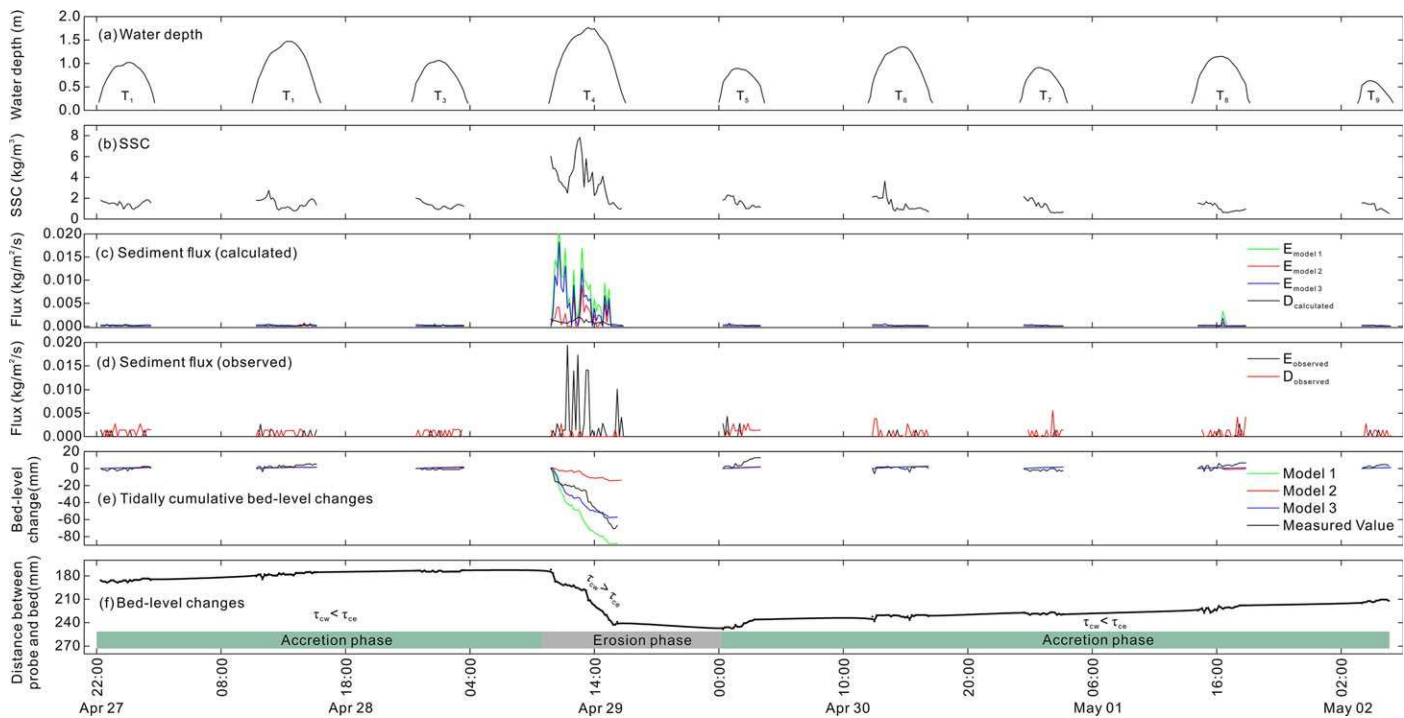
Figure 10. (a) Water depth, (b) suspended sediment concentration (SSC), (c) sediment flux (calculated), (d) sediment flux (observed), (e) tidally cumulative bed-level changes, and (f) bed-level changes during the period of field measurements (27 April to 2 May 2013). T_1–T_9 indicate a series of tides during the field measurements. In Figure 10d, $E_{observed}$ and $D_{observed}$ are defined as dry sediment mass per unit horizontal area per unit time produced by measured erosion and deposition, respectively. Water depths of <0.2 m indicate that effective data recording stopped because the instrument sensors were exposed to air.

tidal cycle were taken into account (index I_{ag} = 0.86; Table 6). When changes under very shallow-water conditions are not considered, values predicted by Model 1 and Model 3 show a lower level of agreement (index I_{ag} = 0.72 for Model 1 and 0.61 for Model 3). Model 2 showed a poorer performance, with the lowest agreement (index I_{ag} = 0.30) obtained when considering only the changes that occurred at water depths of > 0.2 m (Table 6). In addition, based on the root-mean-square error (RMSE), correlation coefficient (r^2), and Brier skill score (BSS) between predicted (Models 1–3) and measured cumulative bed-level changes (Table 6), Model 1 showed a better performance when the entire tidal cycle was taken into account using index I_{ag}, BSS and r^2 compared to RMSE.

Table 3
Erosion Flux (E) Based on the Shear Stress Models of van Rijn (1993) (Model 1; E_model 1), Soulsby (1995) (Model 2; E_model 2), Grant and Madsen (1979) (Model 3; E_model 3) and Estimation of Erosion (E_observed), and Deposition Flux (D) Based on Equation (18) (D_calculated) and Estimation of Accretion (D_observed)

| | E (kg/m²/s, ×10⁻³) | | | | | | | | | | | | | | | | | D (kg/m²/s, ×10⁻³) | | | | | |
| | $E_{model\ 1}$ | | | $E_{model\ 2}$ | | | $E_{model\ 3}$ | | | $E_{observed}$ | | | $D_{calculated}$ | | | $D_{observed}$ | | |
Tide	Max	Min	Ave	Max	Min	Ave	Max	Min	Ave	Max	Min	Ave	Max	Min	Ave	Max	Min	Ave
1	0.48	0	0.10	0.37	0	0.05	0.39	0	0.06	1.41	0	0.28	0.28	0.14	0.22	2.73	0	1.08
2	0.69	0	0.11	0.45	0	0.04	0.66	0	0.10	2.64	0	0.33	0.41	0.14	0.22	1.59	0	0.62
3	0.56	0	0.06	0.39	0	0.04	0.32	0	0.02	1.41	0	0.18	0.30	0.11	0.20	1.59	0	0.80
4	22.50	0	6.17	8.84	0	1.72	18.25	0	4.30	19.43	0	3.34	1.96	0.24	0.91	2.73	0	0.25
5	0	0	0	0	0	0	0	0	0	4.32	0	0.55	0.34	0.15	0.23	2.82	0	1.35
6	0	0	0	0	0	0	0	0	0	1.41	0	0.15	0.54	0.10	0.21	3.87	0	0.72
7	0	0	0	0	0	0	0	0	0	1.41	0	0.08	0.33	0.09	0.19	5.55	0	0.81
8	0	0	0	0	0	0	0	0	0	2.73	0	0.22	0.25	0.09	0.16	4.14	0	0.84
9	0	0	0	0	0	0	0	0	0	1.41	0	0.22	0.24	0.08	0.17	2.27	0	0.64

Note. Max = maximum value; Min = minimum value; Ave = average value.
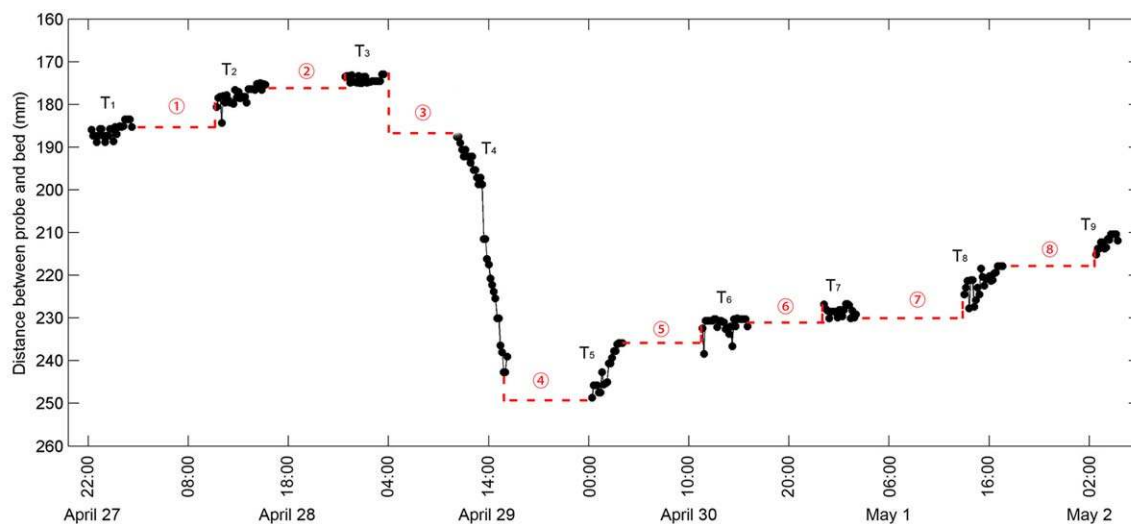
Table 4

Cumulative Bed-Level Change at Water Depths of <0.2 m and >0.2 m for the Total Period of Field Measurements, and Their Percentage Contributions to the Change Over the Entire Tidal Cycle (%) and Duration (min and % of Entire Tidal Cycle)

Water depth < 0.2 m stage				Water depth > 0.2 m stage			
Bed-level changes (mm)	%	Duration (min)	%	Bed-level changes (mm)	%	Duration (min)	%
+14	35	280	11	−40	65	2350	89

Note. "−" denotes erosion, and "+" denotes accretion.

5. Discussion

Our results suggest that morphodynamic changes during VSWS are considerable. These large and rapid changes are most likely attributable to hydrodynamic features and sediment concentrations during very shallow-water conditions. To be more specific, compared with deep-water stages, VSWS are generally characterized by rapidly changing shallow-water flows and a high SSC. Firstly, a tidal front typically occurs, characterized by a significantly variation in bottom velocity from zero up to tens of centimeters per second within a few seconds (i.e., abrupt changes in velocity) (e.g., Gao, 2010; Nowacki & Ogston, 2013). Secondly, VSWS are generally accompanied by a peak value of SSCs, which tend to be the maximum value within the entire tidal cycle (e.g., Zhang et al., 2016), thereby leading to a marked increase in depositional flux based on equation (18). These hydrodynamic and sediment processes are likely to govern morphodynamics in such very shallow-water environments, and could cause the large and rapid bed-level changes as compared

Phases	Bed-level changes (mm)							
	Phase of $h < 0.2$ m				Phase of $h > 0.2$ m			
	Net (mm)	Duration (min)	Rate (×10⁻²) (mm/min)	%	Net (mm)	Duration (min)	Rate (×10⁻²) (mm/min)	%
$h > 0.2$ m (T₁)	/	/	/	/	+0.6	250	+0.2	90.9
$h < 0.2$ m (①)/$h > 0.2$ m (T₂)	+4.7	23	+20.4	7.3	+5.2	290	+1.8	92.7
$h < 0.2$ m (②)/$h > 0.2$ m (T₃)	+1.9	26	+7.3	9.8	+0.6	240	+0.3	90.2
$h < 0.2$ m (③)/$h > 0.2$ m (T₄)	−14.7	22	−66.8	6.6	−51.4	310	−16.6	93.4
$h < 0.2$ m (④)/$h > 0.2$ m (T₅)	−9.7	24	−40.4	11.2	+12.8	190	+6.7	88.8
$h < 0.2$ m (⑤)/$h > 0.2$ m (T₆)	+3.5	20	+17.5	6.7	+0.5	280	+0.2	93.3
$h < 0.2$ m (⑥)/$h > 0.2$ m (T₇)	+5.1	21	+24.3	9.5	+2.3	200	+1.2	90.5
$h < 0.2$ m (⑦)/$h > 0.2$ m (T₈)	+4.6	22	+20.9	8.4	+6.7	240	+2.8	91.6
$h < 0.2$ m (⑧)/$h > 0.2$ m (T₉)	+2.7	24	+11.3	14.6	+3.2	140	+2.3	85.4

Figure 11. Comparison of changes in bed-level between phases of water depth (h) < 0.2 m and h > 0.2 m. The annotations ①–⑧ indicate bed-level changes of h < 0.2 m, and T₁–T₉ indicate a series of tides during the field measurements. Negative denotes erosion, and positive denotes accretion.
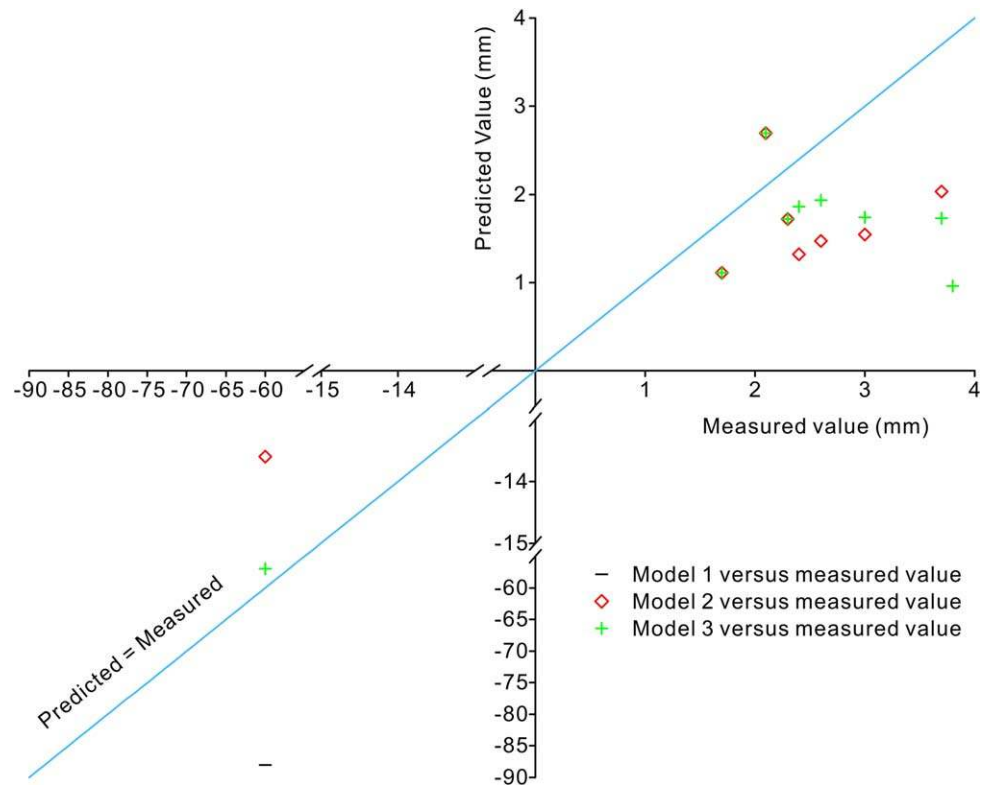
Figure 12. Comparison of predicted and measured values of tidally cumulative bed-level changes. Prediction and measurement of the tidally cumulative bed-level changes were based on the sediment dynamic models of van Rijn (1993) (Model 1), Soulsby (1995) (Model 2), and Grant and Madsen (1979) (Model 3), and on the *in situ* ADV survey, respectively.

with relatively deep-water conditions. This inference is also supported by previous studies (e.g., Bassoullet et al., 2000; Bayliss-Smith et al., 1979; Gao, 2010; Zhang et al., 2016). For example, Gao (2010) showed that a large amount of sediment is deposited on/eroded from on the bottom bed during the very shallow-water period, causing large bed-level changes. Similar results were found by Zhang et al. (2016) on a mudflat south of the Chuandong River, Yancheng City, China, in which the bed shear stresses during VSWS were sufficiently large to re-suspend and transport large amounts of bottom sediment. Thus, these two aforementioned studies are consistent with our results, which show that bed-level changes during VSWS accounted for 35% of the changes in bed-level for the entire tidal cycle (Table 4).
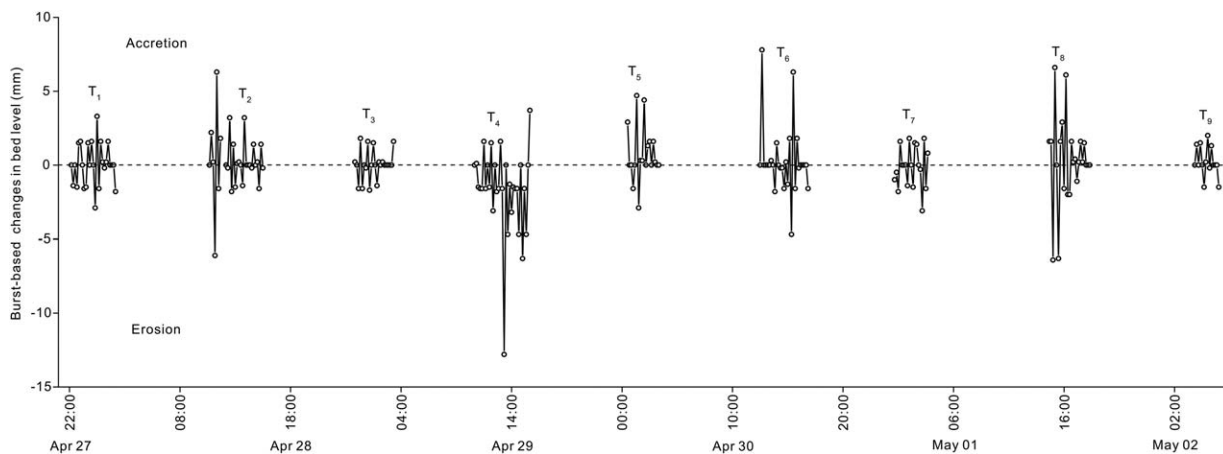

Figure 13. Time series of burst-based changes in bed-level during the field measurements (27 April to 2 May 2013). Negative denotes erosion, and positive denotes accretion.

Table 5
Statistics of the Duration of Water Depth (h) > 0.2 m, Ripple Migration Rate (U$_r$, Equation (3)), Ripple Height (η), Ripple Wavelength (λ), and Maximum Value of Bed-Level Changes (MVBC)

Tide	Duration of h > 0.2 (min)	U$_r$ (cm/min)	η (cm)	λ (cm)	MVBC(cm)
1	250	0.38	1.8	5.5	+0.56
2	290	0.57	1.9	6.3	+0.52
3	240	0.34	1.9	6.3	+0.63
4	310	0.49	2.3	7.4	−5.51
5	190	0.34	2.3	7.4	+1.28
6	280	0.33	1.5	6.2	+0.83
7	200	0.23	1.5	6.2	+0.34
8	240	0.21	/	/	+0.99
9	140	0.19	/	/	+0.35

Note. Ripple height and wavelength were measured *in situ* during the emergence period (after the ebb). MVBC is the maximum magnitude of tidally cumulative bed-level changes (Figure 10e). "/" denotes no ripple measurement data, "−" denotes erosion, and "+" denotes accretion.

Although many erosion–accretion experiments have been conducted using flumes or field instruments (e.g., Amos et al., 1992; Mehta, 1988; Mehta & Partheniades, 1979; Partheniades, 1962, 1965; Whitehouse & Mitchener, 1998; Zhang et al., 2016), few experiments have explored the very shallow morphodynamic characteristics of intertidal flats because of difficulties in carrying out *in situ* measurements of erosion and accretion during VSWS (e.g., Green & Coco, 2014). In this study, we determined that although the VSWS accounted for only 11% of the entire duration of tidal inundation, the bed-level changes in this short period accounted for 35% of the total changes. Thus, a number of important implications for estuarine morphodynamics emerge from our results. Firstly, the large and rapid bed-level changes that occur during very shallow flow conditions are likely to play an important role in micro-topography formation and destruction. Table 1 lists changes in ripple height that are likely linked to bed-level changes that occurred during VSWS. Our reasoning is as follows. The results show that during the accretion phase (Tides 1–3 and 5–9) the accretion rate in very shallow flows was higher than during deep flows (Figure 11), suggesting that the former was characterized by relatively weak turbulence compared with the latter. In contrast, during the erosion phase (Tide 4), turbulence was likely stronger during very shallow flows, because the erosion rate was
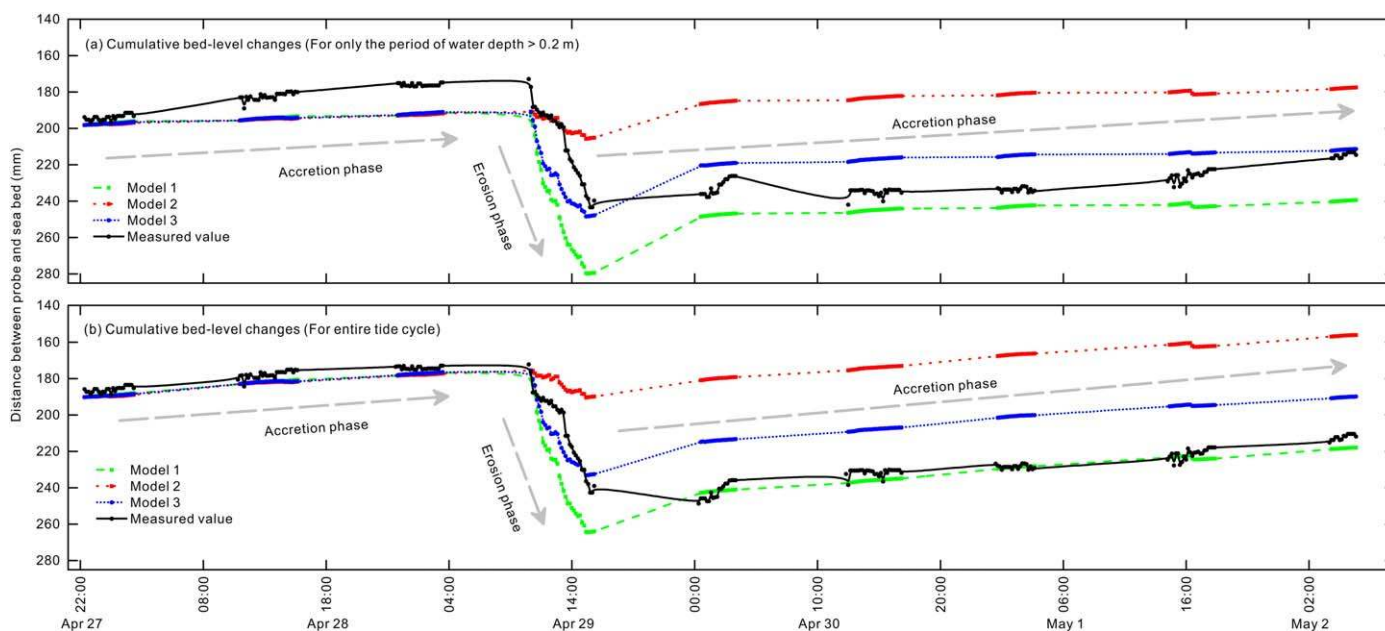

Figure 14. Comparison between time series of measured and predicted cumulative bed-level changes for the period of water depth > 0.2 m (a) and the entire tidal cycle (b).

Table 6

Inter-Comparison of Index of Agreement (I$_{ag}$, Willomott Model), Root-Mean-Square Error (RMSE), Correlation Coefficient (r^2) and Brier Skill Score (BSS) Between Predicted (Model 1–3) and Measured Cumulative Bed-Level Changes

	Models	I$_{ag}$	RMSE	r^2	BSS
Only considering the period of water depth > 0.2 m	Model 1	0.72	24.35	0.85	−0.36
	Model 2	0.30	36.76	0.54	−1.41
	Model 3	0.61	25.54	0.82	−0.10
Considering the entire tidal cycle	Model 1	0.81	21.43	0.93	0.16
	Model 2	0.36	43.35	0.56	−1.95
	Model 3	0.86	25.60	0.84	−0.09

Note. A Brier skill score (BSS) of 1.0 indicates a perfect probability forecast, whereas a BSS of 0.0 indicates the skill of the reference forecast, and a BSS < 0.0 indicates that the mean of the measured values is a better predictor than that produced by a given model.

higher (Figure 11). However, numerous studies have found that ripples develop as a result of local turbulent events acting across the interface between the erodible bed and water (e.g., Bartholdy et al., 2015; Bose & Dey, 2012; Coleman & Melville, 1996; Raudkivi, 1963; Williams & Kemp, 1971), with ripple formation and destruction being linked to local bursting events such as sweeps and ejections (e.g., Best, 1992; Gyr & Schmid, 1989; Keshavarzi et al., 2012; Schindler & Robert, 2005). Thus, we can infer that the high accretion rate and relatively weak turbulence of VSWS during the accretion phase would lead to a decrease in ripple height (Table 1; ripple destruction), whereas the high erosion rate and relatively strong turbulence of VSWS during the erosion phase would lead to an increase in ripple height (Table 1; ripple formation). As such, our understanding of ripple development and destruction under very shallow-water conditions, as described above, supports the contention that sediment dynamic processes during VSWS play a significant role in the development and formation of micro-topographic features, such as small sand ripples and grooves (e.g., Gao, 2010; Zhang et al., 2016; Zhou et al., 2014). These micro-topographic features may promote the formation of larger geomorphological units, such as large tidal creeks (e.g., Zhou et al., 2014).

Accurate quantification of erosion and accretion is useful for deriving a time-series of bed-level changes. There are many uncertainties in measurements of bed-level changes in a highly turbid estuarine environment (e.g., Miao, 2016; Shi et al., 2012). The first reason for this is the universal presence of a fluid-like mud layer due to the effect of high SSCs on intertidal flats (e.g., Andersen et al., 2006; Yang et al., 2003, 2005; Shi et al., 2017). This is supported by observations on another mudflat in the Yangtze delta front, where >10 kg/m^3 of near-bed SSC can be generally observed, even during normal weather (Miao, 2016; Figure 15). However, the presence of a fluid-like mud is unlikely to be an issue in our study, because the bed-level changes were measured using ADV. An ADV was utilized to measure bed-level changes, not only due to its high accuracy (±1 mm) (e.g., Andersen et al., 2007; Salehi & Strom, 2012; Shi et al., 2015), but also because it is able to detect the interface between the water mass and sediment bed. ADV is based on acoustic rather than optical principles (e.g., Lohrmann et al., 1994; Maa et al., 1997; Poindexter et al., 2011; Shi et al., 2017; Voulgaris & Trowbridge, 1998) and, unlike optical instruments, ADV measurements of bed levels are not
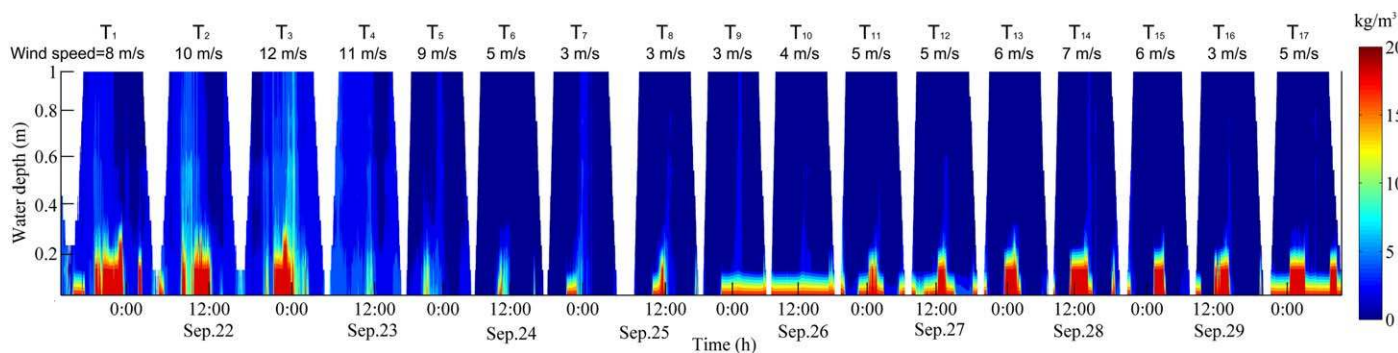

Figure 15. Vertical distribution of suspended sediment concentrations (SSC) at different wind speeds in the Luchaogang mudflat at the Yangtze delta front (22–29 September 2014). Modified after Miao (2016).

affected by near-bed fluid-like mud. For example, in January and November 2005 on the Kongsmark mud-flat in the Lister Dyb tidal basin, Danish Wadden Sea, Andersen et al. (2007) have measured the time-series of bed-level changes in the presence of maximum SSC values as high as $2.5 - 3.0$ kg/m^3 (Figures 4 and 5 in the Andersen et al. (2007)), which is similar to most of SSC values at the present study site (Figure 10b), suggesting that ADV bed-level instrument could be insensitive to the impact of high SSCs. Hence, ADV has been successfully used in many studies of mudflat bed-level changes (e.g., Andersen et al., 2006, 2007; Ha et al., 2009; Shi et al., 2015, 2017).

In terms of bed elevation determination, bedform migration, tripod subsidence, or scour around the tripod legs may also generate erosion–accretion-like records. Here we are particularly concerned with bedform migration that causes periodic changes in the bed elevation record. In this study, the estimations of burst-based changes and maximum value of bed-level changes (MVBC) can be evaluated to distinguish between bed-level changes and the ripple migration effect (equations (1) and (3); Table 5 and Figure 13). During field measurements, the ripple wavelength (λ) was ca. 6 cm and ripple migration (U_r) ranged from 0.19 to 0.57 cm/min (Table 5), implying that the probe periodically recorded a large number of crest-to-trough changes. However, the MVBC was always less than the ripple height of the corresponding tide during Tides 1–3 and 5–9 (Table 5), and burst-based elevation changes were less than ripple height for all tides (Figure 13), suggesting that measurements of bed elevation were not related to ripple migration. Although we did not observe ripple migration rates, the effect of migrating ripples on the *in situ* measurements of bed-level changes is of secondary importance (equations (1) and (3); Table 5 and Figure 13).

Future work should include studies of the physical mechanisms that underlie the relationship between hydrodynamics and the development of micro-topography during VSWS. This needs more detailed time-series of erosion and accretion processes and hydrodynamic data during VSWS. Thus, it also requires an instrument with a shorter standoff that can be submerged within shallow water, providing higher-resolution (both temporal and spatial) bed-level measurements to adequately characterize the complex morphological changes that occur in intertidal mudflats. In addition, more numerical modeling is needed of morphodynamic behavior and sediment transport during VSWS. The present models have limitations in very shallow water because of difficulties in accounting for complicated sediment exchange and strong turbulent mixing processes in such shallow-water environments.

6. Conclusions

Field experiments have quantified how very shallow-water flows affect the morphological change of inter-tidal mudflats. We have conducted integrated and continuous measurements of waves, near-boundary current velocities, SSCs, and bed-level changes on the Wanggang mudflat, Jiangsu coast, China. These measurements and modeled time-series of bed-level changes were used to examine bed-level changes within entire tidal cycles, and to determine the importance of changes in bed-level during VSWS.

Our results showed that VSWS accounted for only 11% of the duration of the entire tidal cycle, but accounted for 35% of the bed-level changes. This result provides insights into micro-topography formation and erosion–accretion processes within an entire tidal cycle. The level of agreement between modeled and measured changes indicates that the hydrodynamic model performed better when the entire tidal cycle was considered, as opposed to when only the submerged phase was modeled. There are three main implications of these results. Firstly, the magnitude of bed-level change during VSWS cannot be neglected when predicting morphodynamic processes. Secondly, the large and rapid bed-level changes that occur during very shallow-flow conditions are likely to play an important role in micro-topography formation and destruction. Finally, future work should focus on the underlying physical links between hydrodynamics, sediment dynamics, and the development of micro-topography during VSWS. More generally, VSWS are an important control on bed-level changes that influence sediment dynamics and benthic habitat availability. As such, this is an important frontier in estuarine research.

Appendix A: Calculation of Critical Shear Stresses

Bottom sediment samples from the Wanggang mudflat (the study site) consist of fine sediments (median grain sizes of 68.1 to 75.7 μm; Table 1). Thus, based on the recommendation of Taki (2001), we determined

the non-dimensional critical shear stress for erosion of bottom sediments (τ_{cr}) using equation (A1), which is suitable for fine sediments with grain sizes less than several tens of microns and relatively high water contents:

$$\tau_{cr} = 0.05 + \beta \left\{ \frac{1}{[(\pi/6)(1+sW)]^{1/3} - 1} \right\}^2 \tag{A1}$$

where β is a dimensionless coefficient (0.3) with values in the range of 0.1 to 2.0, with a mean value 0.3 according to Taki (2001), s is a dimensionless unit defined as the ratio of the density of the sediment particle to the density of water ($= \rho_s/\rho_w$), i.e., relative density of the sediment, ρ_s is the sediment particle density (2,650 kg/m^3), ρ_w is seawater density (1,030 kg/m^3), and W is the water content ($W = 32$ in this study, with the same definition as Taki (2001), i.e., the percentage of water mass divided by dry sediment mass, and water weight denotes the difference between the wet and dry weights, as measured in the laboratory). Then the non-dimensional critical shear stress (τ_{cr}) is 0.10. Using the relationship provided by Shields (1936) and Soulsby (1997) the dimensional value (τ_{ce}) becomes 0.11 N/m^2.

References

Abuodha, P. A., & Woodroffe, C. D. (2006). Assessing vulnerability of coasts to climate change: A review of approaches and their application to the Australian coast. In C. Woodroffe, E. Bruce, M. Puotinen, & R. Furness (Eds.), *GIS for the coastal zone: A selection of papers from CoastGIS 2006*. Wollongong, NSW: Australian National Centre for Ocean Resources and Security University of Wollongong.

Amos, C. L., Daborn, G. R., Christian, H. A., Atkinson, A., & Robertson, A. N. D. A. (1992). In situ erosion measurements on fine–grained sediments from the Bay of Fundy. *Marine Geology*, *108*, 175–196. https://doi.org/10.1016/0025-3227(92)90171-D

Andersen, T. J., Fredsoe, J., & Pejrup, M. (2007). In situ estimation of erosion and deposition thresholds by Acoustic Doppler Velocimeter (ADV). *Estuarine Coastal Shelf Science*, *75*, 327–336. https://doi.org/10.1016/j.ecss.2007.04.039

Andersen, T. J., Pejrup, M., & Nielsen, A. A. (2006). Long-term and high-resolution measurements of bed level changes in a temperate, microtidal coastal lagoon. *Marine Geology*, *226*(1), 115–125.

Bale, A. J., Widdows, J., Harris, C. B., & Stephens, J. A. (2006). Measurements of the critical erosion threshold of surface sediments along the Tamar Estuary using a mini–annular flume. *Continental Shelf Research*, *26*, 1206–1216. https://doi.org/10.1016/j.csr.2006.04.003

Balke, T., Herman, P. M., & Bouma, T. J. (2014). Critical transitions in disturbance–driven ecosystems: Identifying Windows of Opportunity for recovery. *Journal of Ecology*, *102*(3), 700–708.

Barbier, E. B. (2013). Valuing ecosystem services for coastal wetland protection and restoration: Progress and challenges. *Resources*, *2*, 213–230. https://doi.org/10.3390/resources2030213

Bartholdy, J., Ernstsen, V. B., Flemming, B. W., Winter, C., Bartholomä, A., & Kroon, A. (2015). On the formation of current ripples. *Scientific Reports*, *5*.

Bassoullet, P., Hir, P. L., Gouleau, D., & Robert, S. (2000). Sediment transport over an intertidal mudflat: Field investigations and estimation of fluxes within the "baie de marenngres-oleron" (france). *Continental Shelf Research*, *20*(12), 1635–1653.

Bayliss-Smith, T. P., Healey, R., Lailey, R., Spencer, T., & Stoddart, D. R. (1979). Tidal flows in salt marsh creeks. *Estuarine and Coastal Marine Science*, *9*(3), 235–255.

Best, J. I. M. (1992). On the entrainment of sediment and initiation of bed defects: Insights from recent developments within turbulent boundary layer research. *Sedimentology*, *39*(5), 797–811.

Bird, E. C. F. (1986). *Coastline changes* (219 pp.), New York, NY: John Wiley.

Biron, P. M., Robson, C., Lapointe, M. F., & Gaskin, S. J. (2004). Comparing different methods of bed shear stress estimates in simple and complex flow fields. *Earth Surface Processes and Landforms*, *29*(11), 1403–1415.

Black, K. S. (1998). Suspended sediment dynamics and bed erosion in the high shore mudflat region of the humber estuary, UK. *Marine Pollution Bulletin*, *37*(37), 122–133.

Bose, S. K., & Dey, S. (2012). Instability theory of sand ripples formed by turbulent shear flows. *Journal of Hydraulic Engineering*, *138*(8), 752–756.

Bouma, T. J., van Belzen, J., Balke, T., van Dalen, J., Klaassen, P., Hartog, A. M., . . . Herman, P. M. J. (2016). Short-term mudflat dynamics drive long-term cyclic salt marsh dynamics. *Limnology and Oceanography Methods*, *61*(6), 2261–2275.

Bowden, K. F., & Fairbairn, L. A. (1956). Measurements of turbulent fluctuations and Reynolds stresses in a tidal current. *Proceedings of the Royal Society of London A: Mathematical, Physical and Engineering Sciences, the Royal Society*, *237*(1210), 422–438.

Chen, J. Y., & Chen, S. L. (2002). Estuarine and coastal challenges in China. *Chinese Journal of Oceanology and Limnology*, *20*, 174–181.

Chung, C. H., Zhuo, R. Z., & Xu, G. W. (2004). Creation of Spartina plantations for reclaiming Dongtai, China, tidal flats and offshore sands. *Ecological Engineering*, *23*, 135–150. https://doi.org/10.1016/j.ecoleng.2004.07.004

Coleman, S. E., & Melville, B. W. (1996). Initiation of bed forms on a flat sand bed. *Journal of Hydraulic Engineering*, *122*(6), 301–310.

Costanza, R., Pérez–Maqueo, O., Martinez, M. L., Sutton, P., Anderson, S. J., & Mulder, K. (2008). The value of coastal wetlands for hurricane protection. *Journal of Human Environment*, *37*, 241–248. https://doi.org/10.1579/0044-7447(2008)37[241:TVOCWF]2.0.CO;2

Dai, Z. J., Liu, J. T., Fu, G., & Xie, H. (2013). A thirteen–year record of bathymetric changes in the North Passage, Changjiang (Yangtze) estuary. *Geomorphology*, *187*, 101–107. https://doi.org/10.1016/j.geomorph.2013.01.004

Davies, A. G., & Thorne, P. D. (2005). Modeling and measurement of sediment transport by waves in the vortex ripple regime. *Journal of Geophysical Research*, *110*, C05017. https://doi.org/10.1029/2004JC002468

Day, J. W., Jr., Boesch, D. F., Clairain, E. J., Kemp, G. P., Laska, S. B., Mitsch, W. J., . . . Whigham, D. F. (2007). Restoration of the mississippi delta: Lessons from hurricanes katrina and rita. *Science*, *315*(5819), 1679.

Dyer, K. R. (2000). Preface (properties of intertidal mudflats). *Continental Shelf Research*, *20*, 1037–1038.

Dyer, K. R., Christie, M. C., Feates, N., Fennessy, M. J., Pejrup, M., & van der Lee, W. (2000). An investigation into processes influencing the morphodynamics of an intertidal mudflat, the Dollard estuary, the Netherlands: I. Hydrodynamics and suspended sediment. *Estuarine Coastal Shelf Science*, *50*, 607–625.

Eisma, D. (1998). *Intertidal deposits: River mouth, tidal flats, and coastal lagoons* (459 pp.). Boca Raton, FL: CRC Press.

Fagherazzi, S., & Mariotti, G. (2012). Mudflat runnels: Evidence and importance of very shallow flows inintertidalmorphodynamics. *Geophysical Research Letters*, *39*, L14402. https://doi.org/10.1029/2012GL052542

Feddersen, F., Gallagher, E. L., Guza, R. T., & Elgar, S. (2003). The drag coefficient, bottom roughness, and wave-breaking in the nearshore. *Coastal Engineering*, *48*(3), 189–195.

Feng, X., & Tsimplis, M. N. (2014). Sea level extremes at the coasts of China. *Journal of Geophysical Research Oceans*, *119*, 1593–1608. https://doi.org/10.1002/2013JC009607

Floyd, I. E., Smith, S. J., Scott, S. H., & Brown, G. L. (2016). Flocculation and settling velocity estimates for reservoir sedimentation analysis. engineer research and development center Vicksburg MS Vicksburg United States.

French, C. E., French, J. R., Clifford, N. J., & Watson, C. J. (2000). Sedimentation–erosion dynamics of abandoned reclamations: The role of waves and tides. *Continental Shelf Research*, *20*, 1711–1733. https://doi.org/10.1016/S0278-4343(00)00044-3

Gao, S. (2010). Extremely shallow water benthic boundary layer processes and the resultant sedimentological and morphological characteristics [in Chinese]. *Acta Sedimentologica Sinica*, *28*, 926–932.

Gedan, K. B., Kirwan, M. L., Wolanski, E., Barbier, E. B., & Silliman, B. R. (2010). The present and future role of coastal wetland vegetation in protecting shorelines: Answering recent challenges to the paradigm. *Climatic Change*, *106*, 7–29. https://doi.org/10.1007/s10584-010-0003-7

Gornitz, V. M., Daniels, R. C., White, T. W., & Birdwell, K. R. (1994). The development of a coastal risk assessment database: Vulnerability to sea–level rise in the U.S. Southeast. *Journal of Coastal Research*, *12*, 327–338.

Grant, J. (1983). The relative magnitude of biological and physical sediment reworking in an intertidal community. *Journal of Marine Research*, *41*(4), 673–689.

Grant, W. D., & Madsen, O. S. (1979). Combined wave and current interaction with a rough bottom. *Journal of Geophysical Research*, *84*, 1797–1808.

Green, M. O., & Coco, G. (2014). Review of wave-driven sediment resuspension and transport in estuaries. *Reviews of Geophysics*, *52*, 77–117. https://doi.org/10.1002/2013RG000437

Gyr, A., & Schmid, A. (1989). The different ripple formation mechanism. *Journal of Hydraulic Research*, *27*(1), 61–74.

Ha, H. K., Hsu, W. Y., Maa, J. Y., Shao, Y. Y., & Holland, C. W. (2009). Using ADV backscatter strength for measuring suspended cohesive sediment concentration. *Continental Shelf Research*, *29*(10), 1310–1316.

Hall, S. J. (1994). Physical disturbance and marine benthic communities: Life in unconsolidated sediments. *Oceanography and Marine Biology: An Annual Review*.

Herman, P. M. J., Middelburg, J. J., & Heip, C. H. R. (2001). Benthic community structure and sediment processes on an intertidal flat: Results from the ECOFLAT project. *Continental Shelf Research*, *21*, 2055–2071. https://doi.org/10.1016/S0278-4343(01)00042-5

Houwing, E. J. (1999). Determination of the critical erosion threshold of cohesive sediments on intertidal mudflats along the Dutch WaddenSea coast. *Estuarine, Coastal and Shelf Science*, *49*(4), 545–555.

Huntley, D. A., & Hazen, D. G. (1988). Seabed stresses in combined wave and steady flow conditions on the Nova Scotia continental shelf: Field measurements and predictions. *Journal of Physical Oceanography*, *18*(2), 347–362.

Janssen–Stelder, B. (2000). The effect of different hydrodynamic conditions on the morphodynamics of a tidal mudflat in the Dutch Wadden Sea. *Continental Shelf Research*, *20*, 1461–1478. https://doi.org/10.1016/S0278-4343(00)00032-7

Joshi, S., Duffy, G. P., & Brown, C. (2017). Critical bed shear stress and threshold of motion of maerl biogenic gravel. *Estuarine, Coastal and Shelf Science*, *194*, 128–142.

Jumars, P. A., & Nowell, A. R. (1984). Fluid and sediment dynamic effects on marine benthic community structure. *American Zoologist*, *24*(1), 45–55.

Ke, X. (1999). Report for the Tidal Flat Reclamation at the South of Dafeng Harbor, Jiangsu [in Chinese].

Keen, T. R., & Glenn, S. M. (2002). Predicting bed scour on the continental shelf during Hurricane Andrew. *Journal of Waterway, Port, Coastal, and Ocean Engineering*, *128*(6), 249–257.

Keshavarzi, A., Ball, J., & Nabavi, H. (2012). Frequency pattern of turbulent flow and sediment entrainment over ripples using image processing. *Hydrology and Earth System Sciences*, *16*(1), 147–156.

Kim, S. C., Friedrichs, C. T., Maa, J. P. Y., & Wright, L. D. (2000). Estimating bottom stress in tidal boundary layer from acoustic Doppler velocimeter data. *Journal of Hydraulic Engineering*, *126*(6), 399–406.

Le Hir, P., Roberts, W., Cazaillet, O., Christie, M., Bassoullet, P., & Bacher, C. (2000). Characterization of intertidal flat hydrodynamics. *Continental Shelf Research*, *20*, 1433–1459. https://doi.org/10.1016/S0278-4343(00)00031-5

Li, Z., Gao, S., & Chen, S. (2007). Characteristics of tide induced bottom boundary layers over the Dafeng intertidal flats, Jiangsu Province, China [in Chinese]. *Ocean Engineering*, *25*, 212–219.

Liu, Y., Li, M., Mao, L., Cheng, L., & Chen, K. (2013b). Seasonal pattern of tidal-flat topography along the jiangsu middle coast, china, using hj-1 optical images. *Wetlands*, *33*(5), 871–886.

Liu, Y., Li, M., Mao, L., Cheng, L., & Li, F. (2013a). Toward a method of constructing tidal flat digital elevation models with modis and medium-resolution satellite images. *Journal of Coastal Research*, *29*(2), 438–448.

Lohrmann, A., Cabrera, R., & Kraus, N. C. (1994). Acoustic-Doppler velocimeter (ADV) for laboratory use. In Fundamentals and Advancements in Hydraulic Measurements and Experimentation (pp. 351–365). Reston, VA: ASCE.

Lyne, V. D., Butman, B., & Grant, W. D. (1990). Sediment movement along the US east coast continental shelf—I. Estimates of bottom stress using the Grant-Madsen model and near-bottom wave and current measurements. *Continental Shelf Research*, *10*(5), 397–428.

Maa, J. P. Y., Sun, K. J., & He, Q. (1997). Ultrasonic characterization of marine sediments: A preliminary study. *Marine Geology*, *141*(1–4), 183–192.

MacVean, L. J., & Lacy, J. R. (2014). Interactions between waves, sediment, and turbulence on a shallow estuarine mudflat. *Journal of Geophysical Research: Oceans*, *119*, 1534–1553. https://doi.org/10.1002/2013JC009477

Mehta, A. J. (1988). Laboratory studies on cohesive sediment deposition and erosion. In *Physical Processes in Estuaries* (pp. 427–445). Berlin, Germany: Springer.

Mehta, A. J., & Partheniades, E. (1979). Kaolinite resuspension properties, ASCE *J. Hydraulic Division American Society of Civil Engineering*, *104*, 409–416.

Mellor, G. (2002). Oscillatory bottom boundary layers. *Journal of Physical Oceanography*, *32*(11), 3075–3088.

Miao, L. M. (2016). Concentration and transport of suspended sediments over an open macro-tidal flat in the Yangtze Delta, Master's thesis, 14 pp, Shanghai, China (in Chinese).

Miller, D. C., Muir, C. L., & Hauser, O. A. (2002). Detrimental effects of sedimentation on marine benthos: What can be learned from natural processes and rates. *Ecological Engineering*, *19*, 211–232. https://doi.org/10.1016/S0925-8574(02)00081-2

Miller, D. C., & Sternberg, R. W. (1988). Field measurements of the fluid and sediment–dynamic environment of a benthic deposit feeder. *Journal of Marine Research*, 46(4), 771–796.

Möller, I., Kudella, M., Rupprecht, F., Spencer, T., Paul, M., van Wesenbeeck, B., . . . Schimmels, S. (2014). Wave attenuation over coastal salt marshes under storm surge conditions. *Nature Geoscience*, 7, https://doi.org/10.1038/NGEO2251

Möller, I., Spencer, T., French, J. R., Leggett, D. J., & Dixon, M. (2001). The sea–defence value of salt marshes – a review in the light of field evidence from North Norfolk. *Water and Environmental Management*, 15, 109–116. https://doi.org/10.1111/j.1747-6593.2001.tb00315.x

Ni, W. F., Wang, Y. P., Symonds, A. M., & Collins, M. B. (2014). Intertidal flat development in response to controlled embankment retreat: Freiston Shore, The Wash, UK. *Marine Geology*, 355, 260–273. https://doi.org/10.1016/j.margeo.2014.06.001

Nowacki, D. J., & Ogston, A. S. (2013). Water and sediment transport of channel-flat systems in a mesotidal mudflat: Willapa Bay, Washington. *Continental Shelf Research*, 60, S111–S124.

Partheniades, E. (1962). *A study of erosion and deposition of cohesive soils in salt water* (PhD thesis). Berkeley, CA: University of California.

Partheniades, E. (1965). Erosion and deposition of cohesive soils. *Journal of the Hydraulics Division American Society of Civil Engineering*, 105–139.

Poindexter, C. M., Rusello, P. J., & Variano, E. A. (2011). Acoustic Doppler velocimeter-induced acoustic streaming and its implications for measurement. *Experiments in Fluids*, 50(5), 1429–1442.

Pope, N. D., Widdows, J., & Brinsley, M. D. (2006). Estimation of bed shear stress using the turbulent kinetic energy approach—a comparison of annular flume and field data. *Continental Shelf Research*, 26(8), 959–970.

Pratolongo, P. D., Perillo, G. M., & Piccolo, M. (2010). Combined effects of waves and plants on a mud deposition event at a mudflat–saltmarsh edge in the Bahía Blanca estuary. *Estuarine, Coastal and Shelf Science*, 87(2), 207–212.

Raudkivi, A. J. (1963). Study of sediment ripple formation. *Journal of the Hydraulics Division American Society of Civil Engineering*, 89(6), 15–34.

Ren, M. E. (1986). *Tidal mud flat, Modern sedimentation in the coastal and nearshore zones of China* (pp. 78–127). Beijing, China: China Ocean Press.

Ribas, F., Falqués, A., de Swart, H. E., Dodd, N., Garnier, R., & Calvete, D. (2015). Understanding coastal morphodynamic patterns from depth-averaged sediment concentration. *Reviews of Geophysics*, 53, 362–410. https://doi.org/10.1002/2014RG000457

Salehi, M., & Strom, K. (2012). Measurement of critical shear stress of mud mixtures in the San Jacinto estuary under different wave and current combinations. *Continental Shelf Research*, 47, 78–92. https://doi.org/10.1016/j.csr.2012.07.004

Schindler, R. J., & Robert, A. (2005). Flow and turbulence structure across the ripple–dune transition: An experiment under mobile bed conditions. *Sedimentology*, 52(3), 627–649.

Shi, B. W., Wang, Y. P., Du, X. Q., Cooper, J. R., Li, P., Li, M. L., & Yang, Y. (2016). Field and theoretical investigation of sediment mass fluxes on an accretional coastal mudflat. *Journal of Hydro–Environmental Research*, https://doi.org/10.1016/j.jher.2016.01.002

Shi, B. W., Wang, Y. P., Yang, Y., Li, M. L., Li, P., Ni, W. F., & Gao, J. H. (2015). Determination of critical shear stresses for erosion and deposition based on in situ measurements of currents and waves over an intertidal mudflat. *Journal of Coastal Research*, 31, 1344–1356. https://doi.org/10.2112/JCOASTRES-D-14-00239.1

Shi, B. W., Yang, S. L., Wang, Y. P., & Bouma, T. J. (2012). Relating accretion and erosion at an exposed tidal wetland to the bottom shear stress of combined current–wave action. *Geomorphology*, 138, 380–389. https://doi.org/10.1016/j.geomorph.2011.10.004

Shi, B. W., Yang, S. L., Wang, Y. P., Li, G. C., Li, M. L., Li, P., & Li, C. (2017). Role of wind in erosion-accretion cycles on an estuarine mudflat. *Journal of Geophysical Research: Oceans*, 122, 193–206. https://doi.org/10.1002/2016JC011902

Shi, B. W., Yang, S. L., Wang, Y. P., Yu, Q., & Li, M. L. (2014). Intratidal erosion and deposition rates inferred from field observations of hydrodynamic and sedimentary processes: A case study of a mudflat–saltmarsh transition at the Yangtze delta front. *Continental Shelf Research*, 90, 109–116. https://doi.org/10.1016/j.csr.2014.01.019

Shields, A. (1936). Application of similarity principles and turbulence research to bed-load movement. *MittPreuss. Versuchsanstalt Wasserbau Schiffbau*, 26, 5–24.

Soulsby, R. (1997). *Dynamics of marine sands: A manual for practical applications*. London, UK: Thomas Telford.

Soulsby, R. L. (1995). *Bed shear–stress due to combined waves and currents, Advances in coastal morphodynamics* (pp. 4–23). Delft, the Netherlands: Delft Hydraulics.

Soulsby, R. L. (2000). Methods for predicting suspensions of mud (HR Wallingford Rep. TR-104). Wallingford, UK: HR Wallingford.

Soulsby, R. L., & Dyer, K. R. (1981). The form of the near-bed velocity profile in a tidally accelerating flow. *Journal of Geophysical Research*, 86, 8067–8074.

Spearman, J., & Manning, A. J. (2017). On the hindered settling of sand-mud suspensions. *Ocean Dynamics*, 67(3–4), 465–483.

Stapleton, K. R., & Huntley, D. A. (1995). Seabed stress determinations using the inertial dissipation method and the turbulent kinetic energy method. *Earth Surface Processes and Landforms*, 20, 807–815.

Styles, R., & Glenn, S. M. (2002). Modeling bottom roughness in the presence of wave-generated ripples. *Journal of Geophysical Research*, 107(C8), 3110. https://doi.org/10.1029/2001JC000864

Sutherland, J., Walstra, D. J. R., Chesher, T. J., van Rijn, L. C., & Southgate, H. N. (2004). Evaluation of coastal area modelling systems at an estuary mouth. *Coastal Engineering*, 51, 119–142.

Taki, K. (2001). Critical shear stress for cohesive sediment transport. In W. H. McAnally & A. J. Mehta (Eds.), *Coastal and estuarine fine sediment processes* (pp. 53–61). Elsevier Science.

Temmerman, S., De Vries, M. B., & Bouma, T. J. (2012). Coastal marsh die–off and reduced attenuation of coastal floods: A model analysis. *Global and Planetary Change*, 92, 267–274. https://doi.org/10.1016/j.gloplacha.2012.06.001

Tuck, I. D., Bailey, N., Harding, M., Sangster, G., Howell, T., Graham, N., & Breen, M. (2000). The impact of water jet dredging for razor clams, Ensis spp., in a shallow sandy subtidal environment. *Journal of Sea Research*, 43(1), 65–81.

Turner, S. J., Grant, J., Pridmore, R. D., Hewitt, J. E., Wilkinson, M. R., Hume, T. M., & Morrisey, D. J. (1997). Bedload and water column transport and colonisation processes by post–settlement benthic macrofauna: Does infaunal density matter? *Journal of Experimental Marine Biology and Ecology*, 216, 51–75. https://doi.org/10.1016/S0022-0981(97)00090-7

van Rijn, L. C. (1993). *Principles of sediment transport in rivers, estuaries and coastal seas* (2.7, 2.15–2.16 pp.). Amsterdam, the Netherlands: Aqua Publication.

Voulgaris, G., & Trowbridge, J. H. (1998). Evaluation of the acoustic Doppler velocimeter (ADV) for turbulence measurements. *Journal of Atmospheric and Oceanic Technology*, 15(1), 272–289.

Wang, A., Ye, X., Du, X., & Zheng, B. (2014). Observations of cohesive sediment behaviors in the muddy area of the northern Taiwan Strait, China. *Continental Shelf Research*, 90, 60–69.

Wang, X., & Ke, X. (1997). Grain–size characteristics of the extant tidal flat sediments along the Jiangsu coast, China. *Sedimentary Geology*, 112, 105–122. https://doi.org/10.1016/S0037-0738(97)00026-2

Wang, Y., (Ed.). (2002). *Radial sandy ridge field on the continental shelf of the South Yellow Sea* (pp. 1–433) [in Chinese]. Beijing, China: China Environmental Science Press.

Wang, Y. P., Gao, S., & Jia, J. J. (2006). High-resolution data collection for analysis of sediment dynamic processes associated with combined current–wave action over intertidal flats. *Chinese Science Bulletin*, 51(7), 866–877.

Wang, Y. P., Gao, S., Jia, J., Thompson, C. E., Gao, J., & Yang, Y. (2012). Sediment transport over an accretional intertidal flat with influences of reclamation, Jiangsu coast, China. *Marine Geology*, 291, 147–161.

Wang, Y. P., Shi, B. W., Zhang, L., Jia, J. J., Xia, X. M., Zhou, L., . . . Gao, J. H. (2017). Coastline vulnerability assessment in Hainan Island, China. *Acta Oceanologica Sinica*, 1–7. https://doi.org/10.1007/s13131-017-0972-8

Whitehouse, R., Soulsby, R., Roberts, W., & Mitchener, H. (2000). *Dynamics of estuarine muds: A manual for practical applications* (pp. 90–91). London, UK: Thomas Telford.

Whitehouse, R. J. S., & Mitchener, H. J. (1998). *Observations of the morphodynamic behaviour of an intertidal mudflat at different timescales, Sedimentary processes in the intertidal zone* (pp. 255–271). London, UK: Geological Society.

Widdows, J., Pope, N., & Brinsley, M. (2008). Effect of Spartina Anglica stems on near bed hydrodynamics, sediment erodability and morphological changes on an intertidal mudflat. *Marine Ecology Progress Series*, 362, 45–57. https://doi.org/10.3354/meps07448

Williams, P. B., & Kemp, P. H. (1971). Initiation of ripples on flat sediment beds. *Journal of the Hydraulics Division American Society of Civil Engineering*, 97(4), 502–522.

Williams, J. J., Rose, C. P., Thorne, P. D., O'connor, B. A., Humphery, J. D., Hardcastle, P. J., & Wilson, D. J. (1999). Field observations and predictions of bed shear stressesand vertical suspended sediment concentration profiles in wave-current conditions. *Continental Shelf Research*, 19(4), 507–536.

Willmott, C. J., Ackleson, S. G., Davis, R. E., Feddema, J. J., Klink, K. M., Legates, D. R., . . . Rowe, C. M. (1985). Statistics for the evaluation and comparison of models. *Journal of Geophysical Research*, 90, 8995–9005.

Winterwerp, J. C., & van Kesteren, W. G. M. (2004). *Introduction to the physics of cohesive sediment in the marine environment*. Amsterdam, the Netherlands: Elsevier.

Yang, S. L., Friedrichs, C. T., Shi, Z., Ding, P. X., Zhu, J., & Zhao, Q. Y. (2003). Morphological response of tidal marshes, flats and channels of the outer Yangtze River mouth to a major storm. *Estuaries*, 26, 1416–1425. https://doi.org/10.1007/BF02803650

Yang, S. L., Li, P., Gao, A., Zhang, J., Zhang, W. X., & Li, M. (2007). Cyclical variability of suspended sediment concentration over a low-energy tidal flat in Jiaozhou Bay, China: Effect of shoaling on wave impact. *Geo-Marine Letters*, 27(5), 345–353.

Yang, S. L., Zhang, J., Zhu, J., Smith, J. P., Dai, S. B., Gao, A., & Li, P. (2005). Impact of dams on Yangtze River sediment supply to the sea and delta intertidal wetland response. *Journal of Geophysical Research*, 110, F03006. https://doi.org/10.1029/2004JF000271

Yang, Y., Wang, Y. P., Gao, S., Wang, X. H., Shi, B. W., Zhou, L., & Li, G. C. (2016a). Sediment resuspension in tidally dominated coastal environments: New insights into the threshold for initial movement. *Ocean Dynamics*, 66(3), 401–417.

Yang, Y., Wang, Y. P., Li, C., Gao, S., Shi, B., Zhou, L., & Dai, C. (2016b). On the variability of near-bed floc size due to complex interactions between turbulence, SSC, settling velocity, effective density and the fractal dimension of flocs. *Geo-Marine Letters*, 36(2), 135–149.

Ysebaert, T., Herman, P. M. J., Meire, P., Craeymeersch, J., Verbeek, H., & Heip, C. H. R. (2003). Large–scale spatial patterns in estuaries: Estuarine macrobenthic communities in the Schelde estuary, NW–Europe. *Estuarine Coastal Shelf Science*, 57, 335–355. https://doi.org/10.1016/S0272-7714(02)00359-1

Zajac, R. N., & Whitlatch, R. B. (2001). Response of macrobenthic communities to restoration efforts in a New England estuary. *Estuaries*, 24(2), 167–183.

Zhang, Q., Gong, Z., Zhang, C. K., Townend, I., Jin, C., & Li, H. (2016). Velocity and sediment surge: What do we see at times of very shallow water on intertidal mudflats. *Continental Shelf Research*, 113, 10–20. https://doi.org/10.1016/j.csr.2015.12.003

Zhou, Z., Olabarrieta, M., Stefanon, L., D'alpaos, A., Carniello, L., & Coco, G. (2014). A comparative study of physical and numerical modeling of tidal network ontogeny. *Journal of Geophysical Research: Earth Surface*, 119, 892–912. https://doi.org/10.1002/2014JF003092

Zhu, D. K., Ke, X., & Gao, S. (1986). Tidal flat sedimentation of Jiangsu coast [in Chinese with English abstract]. *Journal of Oceanography, Huanghai Bohai Seas*, 4(3), 19–27.